UNIVERSITAT POLITÈCNICA
DE CATALUNYA
BARCELONATECH

Jack Wallis

Exploration and Utilisation of Lunar Resources affected by Space Weathering

Master's Thesis

submitted in partial fulfilment
of the requirements for the degree of

Master of Science in Space and Aeronautical Engineering

Submitted to:

Universitat Politècnica de Catalunya

Supervised by Prof. Ignasi Casanova

Escola Superior d'Enginyeries Industrial, Aeroespacial i
Audiovisual de Terrassa (ESEIAAT)

Terrassa, June 2021

Abstract

This thesis aims to develop a study with regards to the exploration of the lunar surface through the resources produced by space weathering. Space weathering events shall be discussed, in terms of how the physical and chemical characteristics of the lunar regolith is affected. Through hydrogen reduction, the products formed from space weathering interactions shall be produced within the lunar simulants JSC-1 and FJS-3. This is followed up with characterising the processed samples via a Scanned Electron Microscope (SEM) to confirm the formation of npFe^0 and SMFe – a product of space weathering. Thereafter, a preliminary quantification of the presence of npFe^0 and SMFe within one of the samples is obtained through a Mössbauer analysis, this is to provide the basis for future more accurate quantification of npFe^0 and SMFe to be created. In addition to these experiments, an analysis on the samples reflectance within the ultraviolet (UV) region of the electromagnetic spectrum is conducted – finding a preliminary correlation between decreasing reddening gradient and increasing reduction temperatures (the temperature in which the sample was reduced at). Finally, an equation was fitted to this correlation in order to mathematically describe the relationship between the sample's reflectance spectra and reduction temperature (the duration of this reduction was first conducted for 2 hours and then 4 hours). This preliminary mathematical model allows for interpolation of the reddening gradient – a characteristic dependent on the products of space weathering, for both the lunar simulants JSC-1 and FJS-3, when a specific reduction temperature is provided. Ultimately providing the basis for a mathematical model to determine the quantities of npFe^0 and SMFe within the lunar regolith by viewing its corresponding UV reflectance spectra.

Acknowledgements

I would like to take this opportunity to thank Prof. Ignasi Casanova for the tireless tutorship that he has provided throughout this project - in terms of answering my questions, organising the experimental process and assisting in the analysis produced in this thesis. Additionally, I would like to convey my appreciation for the trust that he has given me during the entirety of this research project. This project has truly been eye opening and extremely enjoyable, delving into the depths of lunar exploration and in-situ lunar resources, for this I am ever grateful.

With regards to the technicians that provided guidance during the experimental phase of this project. I want to extend my thanks to: Isabel Serrano Carreño for conducting tutorials and answering the many questions that I had with regards to the hydrogen reduction phase; Trifon Todorov Trifonov for providing tutorials to utilise the UV-3600 spectrometer independently, aiding throughout the characterisation of the lunar samples and serving as a reliable reference when analysing the spectra produced by the lunar simulants; and Pere Bruna Escuer for demonstrating the set up of the Mössbauer analysis, and also for developing the raw data produced from the Mössbauer analysis to the quality in which is seen in this thesis. Without all of their guidance, time and effort, it would have been impossible to conduct the experiments necessary to see the success of this thesis.

Finally, I want to thank the people that provided unconditional support throughout this year and through this research project, my family - my father, mother and sister. Last but not least, I want to thank Amirlan for also providing unconditional support.

Contents

List of Figures

List of Tables

Chapter 1

Introduction

1.1 Aim

The aim of this thesis is to discuss: what is classed as space weathering, the effects that space weathering has on the lunar regolith, and the resources which are present on the lunar surface. With this being defined, experiments shall be taken place to mimic the effects of space weathering by inciting the reduction of iron oxide within the lunar simulants JSC-1 and FJS-3. Once reduction has taken place, the optical spectra will be analysed with the aim to discuss how the products of space weathering impact the optical spectra produced by the lunar simulants. Ultimately accomplishing the main goal of the project - to produce a reference for future remote sensing missions in detecting metallic iron on the lunar surface.

1.2 Scope

To demonstrate clarity, this project's objectives shall be stated, along with the work packages that are essential in order for the success of this research project to be achieved. By accomplishing this, the scope of the project will be defined, allowing for coherency when moving forward throughout this research project.

Primary Objectives

- Discuss the composition and physical characteristics of the lunar surface.
- Defining the term ”space weathering” and how the events classed as space weathering interact with the lunar regolith.
- Demonstrate why the lunar simulants JSC-1 and FJS-3 are suitable substitute for the in-situ samples of lunar regolith.
- Experimentally show that space weathering interactions can be mimicked.
- Display how the optical properties of the lunar simulants alter as the product of space weathering, npFe^0 or SMFe particles, increase within the lunar simulants.
- Provide preliminary quantification of the change in optical properties and the increasing metallic iron with in lunar simulants.

Secondary Objectives

- A discussion shall take place elaborating on the potential this project has in regards to educating the reader in space resources and methods of locating such resources.

- Discuss the future benefits the results from this project will have on the environment.

Followed by this the necessary work packages are defined. As previously mentioned, these work packages present the task in which need to be completed in order to successfully accomplish the specified objectives for this project.

Work Packages

1. **Research**
   - 1.1 Research the characteristics of the lunar regolith
   - 1.2 Research the Composition of the lunar surface, both through the analysis of retrieved samples, and analysis' conducted remote sensing mission obseriving in-situ samples.
   - 1.3 Research the physical and chemical properties of lunar simulants JSC-1 and FJS-3.
   - 1.4 Research the interactions which take place between the lunar surface and space weathering.
   - 1.5 Research the products which are generated through the space weather-lunar surface interaction.
   - 1.6 Research previous experiments which have attempted to mirror the space weather-lunar regolith interaction.
   - 1.7 Research how SMFe and npFe^0 effect optical spectra.
2. **Experiments**
   - 2.1 Conduct hydrogen reduction experiments on the lunar simulants to mimic the interaction of solar wind and the lunar regolith.
   - 2.2 Utilise a Scanned Electron Microscope (SEM) to inspect processed samples.
   - 2.3 Conduct UV-VIS spectroscopy on the processed samples
   - 2.4 Complete Mössbauer analysis on an unprocessed sample and a later selected processed sample
3. **Analysis**
   - 3.1 Analyse the images generated via the SEM to gain preliminary characterisation of the lunar samples and confirm the appearance of SMFe or npFe^0.
   - 3.2 Analyse the optical spectra gained via the UV-VIS spectrometer, determining the alteration in behaviour through the reduction of the simulants.
   - 3.3 Preliminary quantification of the optical spectra with regards to reduction temperature.
   - 3.4 Analyse the data acquired via the Mössbauer analysis, gaining preliminary quantification on the increase in metallic iron when comparing an unprocessed sample to a processed sample.

1.3 Requirements

The requirements for this thesis is as follows:

- Identify the composition of the lunar regolith.

- Identify the composition of the lunar simulants JSC-1 and FJS-3.
- Identify the products of space weathering.
- Discuss how space weathering products effect optical spectra.
- Determine a correlation between space weathering and the optical spectra produced.
- Gain preliminary quantities of the increase in space weathering products produced by the hydrogen reduction experiment.

1.4 Justification

Deep space exploration, such as: exploring the Moon, reaching Mars, or delving deeper into space, becomes an issue as the payload within launchers are limited. Therefore, off-world bases are essential if the human race is to become a space faring civilisation. They offer the ability to provide a housing unite for crew members, and re-supply locations for spacecrafts travelling vast distances through our solar system. However, what is the point of constructing an off world base if missions are not only required, but essential to see that the base stays operational. In the unfortunate case of an extinction level event occurring on Earth these bases would most definitely not survive if still dependent on Earth's resources. Thus, it is essential that we as a civilisation understand and analyse methods in which will see the future utilisation of space resources a reality.

Lunar resources come in many forms, and are proving vitally important as the space industry grows with the demand for further manned exploration missions increases. Being able to locate, extract and utilise resources off-world removes a level of dependency on Earth's own resources. Reducing the need for the transportation and loading of equipment and materials needed for space missions. Understanding this is essential for making it possible for humans to stay in space for longer periods of time, and allows for the possibility to travel further distances in space.

Previous missions have determined the resources which are present on the Moon vary from being minerals and metals to even water. Many studies have discussed the locating and extraction of water and oxygen. For the obvious reason, that these resources are essential for humans to survive anywhere, both on Earth and in space. However, not many have discussed the importance of metallic iron, a resource which will be discussed in depth throughout this study – with regards to its appearance and its characteristics. It could be said that metallic iron is the most important metal used on Earth and subsequently would be an extremely important material for an off-world base. The uses of iron on earth range from being applied in electronics and as construction materials, proving that it will be a vital resource for such missions like the ”Lunar gateway” [1] and ”Artemis” [2] mission, missions that are initialising the re-arrival of humans on Mars.

The Lunar regolith is greatly affected by space weathering in the form of solar winds and micrometeorites impacts [3]. For this reason, an analysis will be conducted on two lunar simulants JSC-1 and FJS-3, where they will be exposed to a hydrogen reduction process, simulating the products which are generated from the space weathering-lunar regolith interactions. Therefore, by analysing the products from this interaction, and viewing how these products effect exploration techniques, exploring the lunar surface for resources will become far less time consuming and costly. For instance, by utilising a

satellite to conduct remote sensing – an exploration technique, the surface area that can be analysed for one satellite can range up to 50% of the total surface of the Moon [4] – an immense area in which would require an extensive project, with a far greater amount of resources to accomplish the same area when just utilising rovers or manned missions. Therefore, this study will conduct an analysis utilising optical spectrometers to quantify a changing behaviour as space weathering products increase – in the hopes that this quantification can act as a reference for future remote sensing mission.

Chapter 2

Review of the State of the Art

This chapter's objective is to define previous experiments and research that have been conducted in this field of interest. By viewing these studies, a consensus will be formed on what to expect from the experiments that will later be applied. Additionally, a basis for referencing will be constructed in order to better analyse the results generated from this study. Through this chapter and the research contained within, a gap in previous studies will be identified, ensuring that the work presented in this study is original and will aid in exploring the lunar surface and methods in which to utilise the lunar resources.

The scope of this research is defined in the previous chapter. For this reason, topics such as the hydrogen reduction, methods of exploring the lunar surface and lunar soil remote sensing shall be discussed. By targeting the essential topics that relate to this project, a solid foundation of knowledge will formed for the future analysis of the results generated via this study.

2.1 Reducing Lunar Samples and Lunar Simulants

Hydrogen reduction is an established method for reducing oxidised iron down to its metallic form – a technique which is being developed to aid in the improvement of the steel industries environmental impact [5]. Many studies have been conducted demonstrating that this is indeed a valid method in reducing lunar regolith. Although, with the majority of them being implemented to obtain water and subsequently oxygen through electrolysis [6, 7, 8, 9], not for the reason of obtaining metallic iron.

In the studies previously referenced, hydrogen is utilised as a reduction agent to produce water and metallic iron, then through electrolysis, the water (H_2O) is separated into its individual composition (hydrogen and oxygen), ultimately gaining oxygen as the final product. This is demonstrated in the next chapter through the chemical equations 3.3 and 3.4, where the theory shall be more specifically discussed. Here, it shall only be clarified that the bi product of these reactions is metallic iron. Hence, it is viable to analyse these papers and their results, due to the fact the production of water and oxygen directly correlates to the production of metallic iron.

But why utilise hydrogen as a reduction agent? In [6] two reduction agents are implemented in an attempt to produce oxygen from ilmenite. These two agents are hydrogen and carbon monoxide, where it is determined that the activation energy for these agents are 22.3 kcal/mole (for hydrogen) and 29.6 kcal/mole (for carbon monoxide). Illustrating that hydrogen requires less energy to reduce ilmenite. Furthermore, hydrogen was

discovered to reduce the ilmenite at a much faster rate when compared to that of carbon monoxide. Therefore, based off of this study hydrogen has the capability to reduce ilmenite, and subsequently the lunar regolith, at lower temperatures and at a reduced energy cost. Backing up the choice for utilising hydrogen as reduction agent when aiming to produce metallic iron from the lunar simulant. Later in this study a detailed discussion will be provided on how the presence of metallic iron correlates to space weathering, further cementing the decision to implement hydrogen as the reduction agent

Additionally, it is important to determine the factors that will impact the reduction process. By viewing the previous experiments conducted by other parties, knowledge on how the lunar regolith's physical characteristics impact the products formed from the reduction process can be established. In [7], ilmenite was reduced via hydrogen in a static reaction chamber. The aim of this paper is to compare how the mass of the ilmenite would effect the oxygen yield. This reaction was conducted at near vacuum pressures. Due to the fact that all samples were reduced under the same conditions, the validity to analyse this paper still holds. Ultimately, this study determined that by increasing the mass of ilmenite placed in the chamber less reduction takes place. However, it must be reiterated that the experiment conducted takes place in a static chamber, hence the larger samples reduce less due to the limited penetration of the hydrogen gas. In this study, the hydrogen will flow through the sample, providing a better ability to react with all grains within the reactor. Nonetheless, it is important to note that the size of the sample will have an impact on the metallic iron generated through the reaction process implemented in this study.

Most recently NASA developed a study where they utilised lunar simulant JSC-1A [8]. A simulant which is identical to the simulant that will later be studied in this thesis. [8] compared JSC-1A to the behaviour of the lunar simulant LHT-2M both being reduced via hydrogen. One of the main objectives of this study is to understand the relationship between the oxygen yield from the reduction process with parameters such as: sintering/clumping, the reactor pressure and particle size. Furthermore, this study was conducted to gain additional data which will see the further development of a model released in previous reports produced by NASA [10, 11].

Figure 2.1: Conversion rate of lunar samples LHT-2M at a reaction temperature of 1300K with particle sizes in the range of 125μm to 250μm [8].

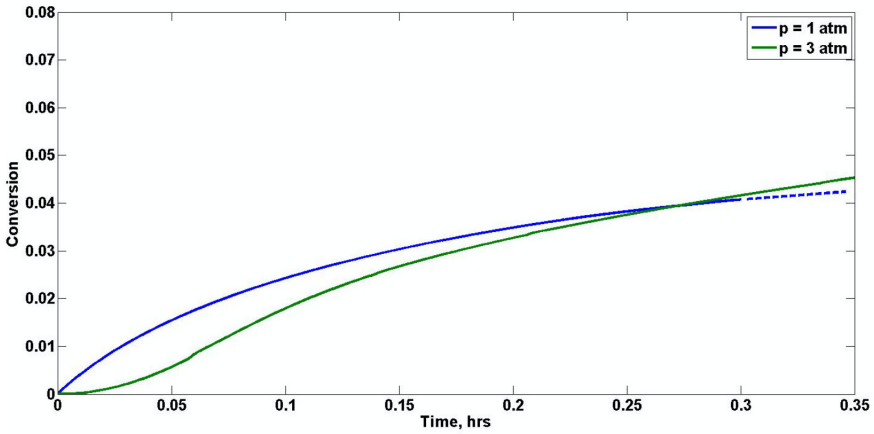

Found through the studies [8, 10, 11], the particle size of the simulant holds an effect on the time before sintering occurs, where smaller particle sizes reduces the time

before sintering occurs. Sintering is also proved to directly correlate with the reduction temperature, proven by quantitatively showing that increased sintering reduces reduction, consequently decreasing the overall efficiency of the entire process. Correlations were also determined between the reactor pressure, and the samples reduction rate. Tests were ran at 1atm and 3atm, finding at higher pressures the conversion rate is initially slower, but as time goes on the conversion rate starts to increase to a rate greater than that seen at 1atm, subsequently producing a greater amount of conversion. Displayed in figure 2.1 is the plot generated from the experiment conducted in [8].

As previously mentioned, these studies aim to further verify a model developed by NASA. This model's objective is to aid in the optimisation of a system that will process in-situ resources on the lunar surface [11]. To improve this optimisation model, proposed through this study, data regarding reduction yield at vacuum pressures would prove to contain very powerful information. This data would indicate the capabilities of the hydrogen reduction process on the lunar surface without inducing a pressure differential between the reactor chamber and the outside environment. Nevertheless, this thesis aims to determine a preliminary view on metallic iron production and the subsequent optical spectra produced. With this being said, all of the studies [8, 10, 11] demonstrate factors like sintering and clumping being a product that must be taken into account within this study due to its effect on the metallic iron yield.

A final comment is to indicate a solution to reduce sintering and clumping, so that its impact on the later ran experiments is minimised. In [8] a flow rate of 1cm/s (under atmospheric conditions) is deemed to be a sufficient flow rate that achieves sample agitation, subsequently minimising sintering and clumping. On top of this, deemed through this same study, if the fluidised sample is not isotropic i.e. equal flow is not occurring through all directions of the sample, sintering and clumping may still occur. Concluding that to reduce sintering and clumping, the flow of the hydrogen will need to be $\geq$1cm/s, and the inlets of the reactor must be clear, ensuring isotropic fluidisation occurs.

Figure 2.2: Reduction rate of ilmenite utilising hydrogen as the reduction agent [6].

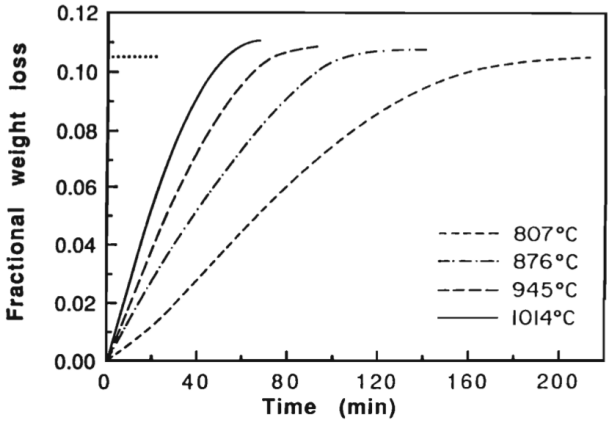

The next factor that must be taken into account is the temperature range which incites reduction to take place. In [7] a reaction temperature of $900°C$ is implemented, as it is referenced from [12] that suitable amounts of oxygen will be produced at this temperature. In [8] a range of temperatures were utilised, ranging from 775°C - 1050°C where reduction takes place throughout the temperature range. In [6] the temperatures implemented

is shown in figure 2.2, presenting how the reduction temperature impacts the total conversion of the sample. Apparent through figure 2.2, reducing ilmentite at a temperature of 1014°C significantly increases the conversion rate than that of the lower reaction temperatures, revealing how reduction temperature has a massive effect on the reduction rate and yield. It must be stated, although this displays a clear relationship between temperature and conversion rate, this experiment was solely conducted on ilmenite, a substance which only makes up 8% of the lunar simulant FJS-3, and is not in the lunar simulant JSC-1 at all. Therefore, as of yet it is not suitable to make the assumption that this relationship is seen as strongly in silicate oxides, the substance which makes up most of the two simulants in question. This study [6] however, provides a reasonable temperature range which can be later implemented within this analysis.

Notably, the studies previously mentioned implemented hydrogen reduction on ilmenite, excluding [8]. Therefor, it will be beneficial to explore another study that analyses a simulant that will be studied in this thesis. Thus, [9] was viewed, a study which analyses the lunar simulant JSC-1, with an objective to complete a thermodynamic analysis on the hydrogen reduction of the lunar simulant. Through this analysis a clear relationship is displayed between the metallic iron produced, the reduction temperature and the reactor pressure, also demonstrating the temperatures in which maximise the metallic iron production. This can be viewed in figure 2.3 where pressure is seen to have a minimal effect on the metallic iron appearance below 1300°C. Additionally, it is seen that the peak of metallic iron yield occurs at 1327°C. Unfortunately, a limitation to the furnace utilised in this analysis sees that the maximum temperature that simulants can be exposed to is 1200°C, this however is not a problem, as it was previously discussed reduction takes place below this temperature.

Figure 2.3: Plot showing metallic Fe conversion efficiency and the corresponding reduction temperature. Additionally showing the effect of the reduction pressure [9]

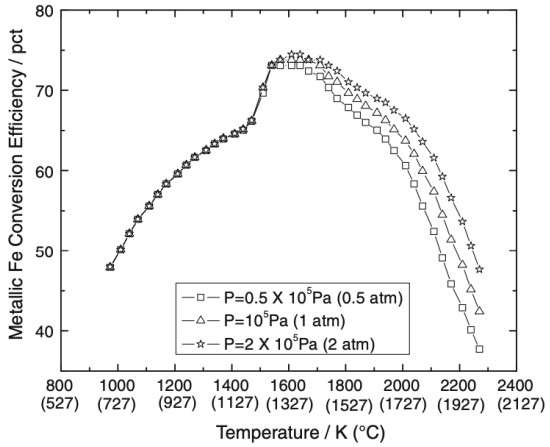

2.2 Utilising Optical Spectroscopy to Exploring the Lunar surface

Remote sensing provides a powerful way to determine the composition of the lunar surface. In order to produce accurate results from a remote sensing mission, analysing the lunar surface, the spectra emitted from lunar simulants must first be accomplished to provide a known reference. Lunar simulants are the next best thing to analysing sam-

ples directly extracted from the Moon. They supply valid results which correspond to the behaviour that is seen from native lunar samples (A comparison that will later be discussed). Nevertheless, the spectra which will be generated through this study must be verified through the previous research that has been conducted. Through the analysis of these previous studies, knowledge will be gained in areas such as how tiny particles of metallic iron impact optical spectra. An effect that was first noted to have a prominent impact in 1975 [13]. Now these metallic iron particle are being frequently referred to as "nanophase iron" (npFe^0) and "submicroscopic iron" (SMFe) [3]. Within this thesis the metallic iron generated from the later implemented reduction process shall be referred to as npFe^0, this is the case when the particle sizes are considered to be smaller than 100nm. SMFe on the other hand, shall be employed as a general term including both metallic iron particles smaller than 100nm and larger.

Many studies have viewed how space weathering impacts the optical spectra of the lunar soil. npFe^0 is a product of space weathering events, which will be later discussed within chapter 3. With this being said, studies that both view how space weathering and npFe^0 or SMFe impact optical spectra will provide a suitable source to gain information with regards to exploring the lunar surface for metallic iron. These studies range from analysing data gained directly from lunar samples, obtained through rovers like the Chang E's [14], or satellites implementing remote sensing tools like the M^3 on board the Chandrayaan-1 [4]; or by evaluating lunar simulants [15].

Models have been produced in order to determine the iron content of the lunar soil and mapping the location of said iron in a global map of the Moon. These studies utilise data gained from telescopes based on here on Earth, or data gathered from satellites such as the Clementine or the Chandrayaan-1. For example, [16] evaluated images gained from the Clementine mission (visit [17] for more information about this mission) and utilised data on locations where the soil compositions were known. Including locations such as the landing sites of the Apollo and the Luna mission in order to create a model which extracts iron oxide content from multispectral images. This model was then later improved through the years producing a global view of the Moon's FeO content [18], constructing an image via Clementine UV/VIS camera published in [19]. Figure 2.4 displays the results produced in [19]. As it can be seen from figure 2.4, the areas which display the densest areas of iron oxide, and most likely metallic iron, coincides with the areas of the maria (the maria corresponds to the darker areas seen on the Moon [20]). The aim of [18] was to map both FeO and TiO_2 utilising and improving upon a model developed in [16]. Concluding that factors such as: grain size, mineralogy, shading due to topography, and the presence of glass – a substance generated from the highly redusive environment on the moon, have an effect on the spectra generated. This study succeeded in improving the algorithm formed in [16], creating an extraction method less sensitive to the maturity of the lunar soil. To summarise, this analysis demonstrates the future potential that analysing optical spectra has on the exploration of the lunar surface. Through inspecting and evaluating, a correlation between the optical reflectance of the lunar simulants tested in this study, and the increasing space weathering products, a detailed mapping of metallic iron, like the one seen in figure 2.4, will be achievable.

As previously mentioned, the model created in [16] disregards the maturity of the soil. This is an issue as the maturity of the soil is a measurement of how long the lunar soil has been exposed to space weathering conditions. Therefore, maturity is directly linked to the presence of npFe^0 and SMFe, and key to quantifying the metallic iron present in the lunar surface. npFe^0 is known to be the dominating factor which alters the spectra generated

Figure 2.4: Global FeO image of the Moon, spatial resolution of 7km/pixel, Lambert equal area projection [18].

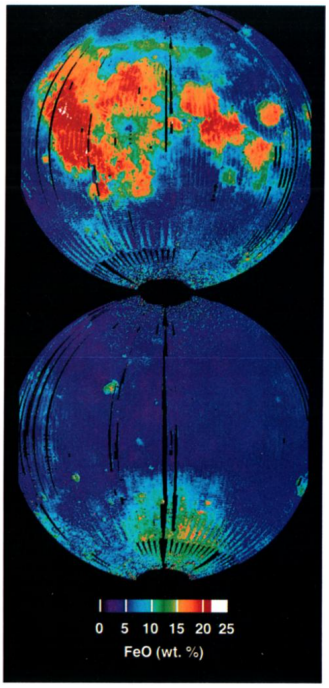

from lunar soils [22]. It is known and proven through experiments and expeditions [23, 3, 14], that reduction of iron to its metallic state both can darken and redden spectra in the visible and infrared region. Similar to the model seen in [18], models have been formed to map the effects of space weathering. For instance, [24] aims to develop a mathematical theory which quantifies the optical effects that are generated by the presence of npFe^0. The model developed in [24] is known as a radiative transfer model and was later tested in [25], where a silica gel containing defined pore sizes housed npFe^0 particles. Through this study, the conclusion is formed that in the visible spectrum, the extinction efficiency of an individual iron particle, decreases with increasing size of the iron particle. Where the high extinction efficiency contributes massively to reddening and darkening of the spectra i.e. as the metallic iron particle increases both its darkening and reddening effects reduce. It was noted, that at particle sizes above 50nm darkening occurred without the reddening effect, which was not implemented into the [24] at the time of this study being completed. Figure 2.5 displays the relationship between the metallic iron particle size and its optical spectra. This present a clear visualisation of the relationship between optical reflectance and metallic iron particle size, and will prove to be essential when analysing the data generated through this thesis.

Previously mentioned, the ”host grain” used in [25] is a transparent silica gel. A substance that is only aimed to house different amounts of npFe^0, not to mimic chemical composition or physical characteristics of the lunar soil. Nevertheless, it provides important information with regards to how the size of npFe^0 and soil maturity effect the optical spectra. With this being said, studies which directly evaluate lunar soil must be taken into account. In [14] the objective is to implement Hapke's radiative model [24] to compute the abundance of SMFe in the lunar soil through data gathered from Chang'E 4. Obtaining spectra within the range of 450nm to 2,395nm, by utilising a VIS/NIR imager and SWIR detector [26]. Successfully quantifying the SMFe at 0.32wt%, with an error of $\pm$0.06wt%, categorising the soil analysed by Chang'E 4 as submature and quantifying the soils ma-

Figure 2.5: Reflectance of iron particles and their particle size for a bright host with a single scattering albedo of 0.99. 0.5wt% of SMFe [21]

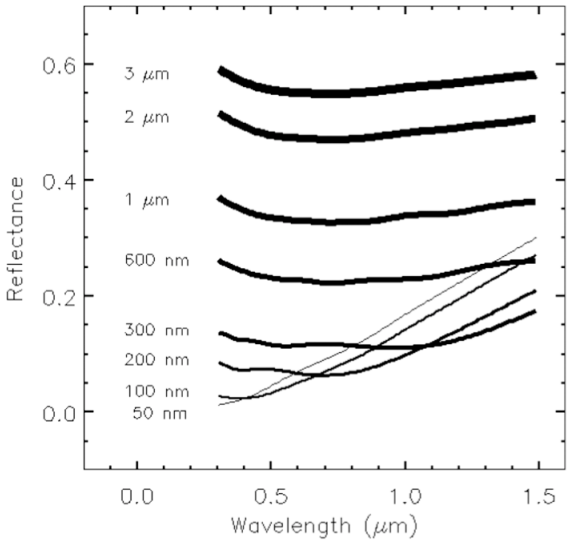

turity on the I_S/FeO index at 82±15. The I_S/FeO index is a widely used maturity index, categorising immature soil in the range of $0.0 < I_S/FeO < 29.0$, submature soils $30.0 < I_s/FeO < 59.0$, and mature $I_s/FeO > 60.0$ [27].

The Chang'E 4 rover landed at the Von Kármán crater in the South Pole-Aitken basin. By viewing figure 2.4, a global view of the Moon, the soil located here is categorised as highland and basin ejecta soil, the other two soil types present on the surface of the Moon. Demonstrating consistency with the sample compositions displayed in table 3.5. Evidently, the data produced by Hapke's radiative model [24] provides an accurate estimation of the lunar regolith's SMFe content when viewing the lunar surface within the visible - Near Infrared region of the electromagnetic spectrum.

Moving forward, the optical spectra of the lunar simulants and mare will be viewed in order to demonstrate the known optical characteristics of both the lunar simulants and the mare itself. This is vital, as it will later be discussed, the lunar simulants studied within this thesis replicates the lunar mare. The area of the lunar surface which contains the densest quantities of iron oxide. In [15] this was accomplished, obtaining spectra of various lunar simulants (JSC-1A and FJS-1) and lunar samples (Apollo 12001 mare and Apollo 64801 highland). As ilmenite is spectrally neutral in the visible and near infrared wavelengths and increases in reflectancy in wavelengths less than 450nm [28], FJS-1 can be used as example of how the FJS-3 will reflect in wavelengths above 450nm. Although, highland soils won't be studied in this thesis, a point made in [14] stats how the natural state of the lunar soil seen on the lunar surface may differ the optical characteristics produced, this is proposed to be due to the fact that the samples extracted from the lunar surface disrupt the upper layer of the soil. By comparing the figure produced from both [15] and [14] this provides and opportunity to determine if any optical properties do alter from in-situ measurements and sample measurements. Figure 2.6b displays the spectra recorded from a Apollo highland sample from [15], clearly showing the same reddening effect seen in figure 2.6a. In addition the magnitudes of reflectance seen in figure 2.6b are almost double of that in figure 2.6a, this can be explained by how the samples in [15] having been sieved, increasing the overall reflectancy of the sample. This is an effect which was also tested and proven in [15]. It must be said that spectra range defined in both figures

2.6b and 2.7 are in micrometers, this can be seen as an error as earlier in the study the range is specified to be in nanometers.

Figure 2.6: Comparison between in-situ lunar regolith and lunar samples gained from the Apollo missions.

(a) Reflectance Spectra gained through Chang'E 4 rover from the Von Kármán crater in the South Pole-Aitken basin [14].

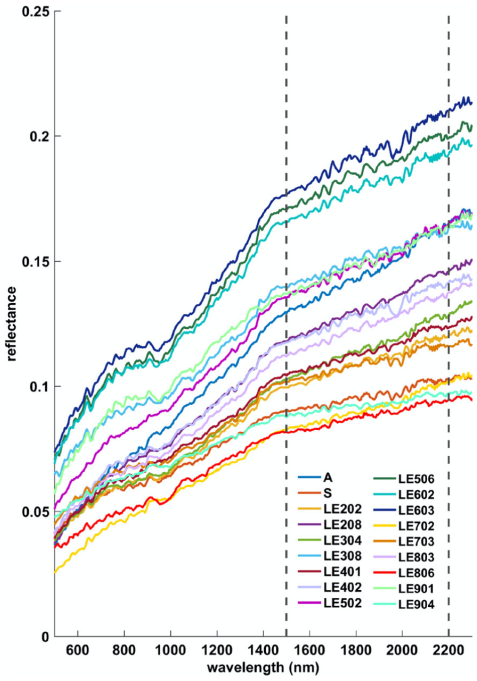

(b) Reflectance of Apollo 64801 highland sample tested in [15] between 250nm and 2,500nm.

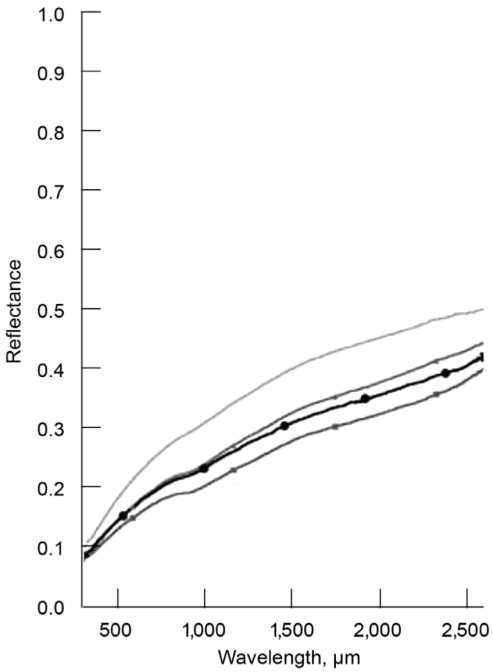

Figure 2.7: Reflectance of simulants tested in [15] between 250nm and 2,500nm.

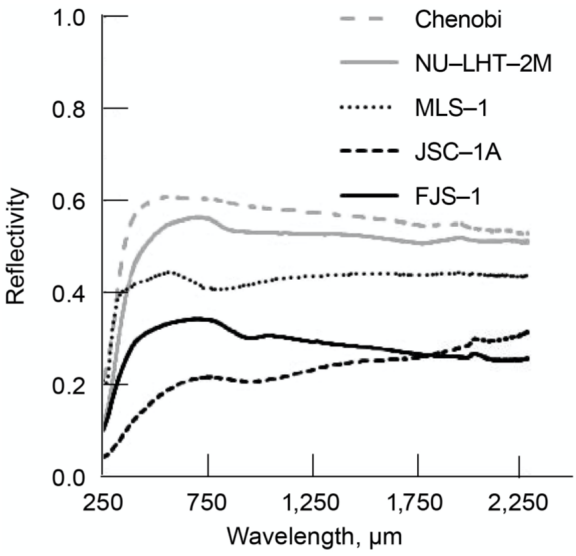

This study [15] aims to determine the optical spectra of the dust present in the lunar regolith and as such sieves the samples to form two categories, 20μm and a 10μm

group. Although, in this thesis the samples shall not be sieved, [15] reveals the optical behaviour of both the lunar samples and the lunar simulants in a wider spectral range to that previously seen in [14]. Through the analysis of this study, the reflectancy of mature JSC-1A displays that the 10μm sample is more absorbent under 500nm, but more reflectant greater than 500nm. Demonstrating how the size of the particles impact the reflectancy of the JSC-1A simulant. Figures2.7 and 2.8 displays the spectra of the simulants and the mare sample spectra. Nevertheless, evident from these figures the simulant JSC-1A offers the closest resemblance to the reflectance spectrum produced from the Apollo 12001 mare sample, demonstrating the same magnitude of refectance and the same reddening slope. FJS-1 however, arrives at a similar magnitude of reflectance at a wavelength of 2,500nm. Evident from figure 2.8 the spectra produced by the sieved samples of 10-20μm, 20-45μm and $<$45μm show absorbance at around 1,000nm, similar to that seen in both JSC-1A and FJS-1 in figure 2.7.

Figure 2.8: Reflectance of Apollo 12001 mare sample tested in [15] between 250nm and 2,500nm.

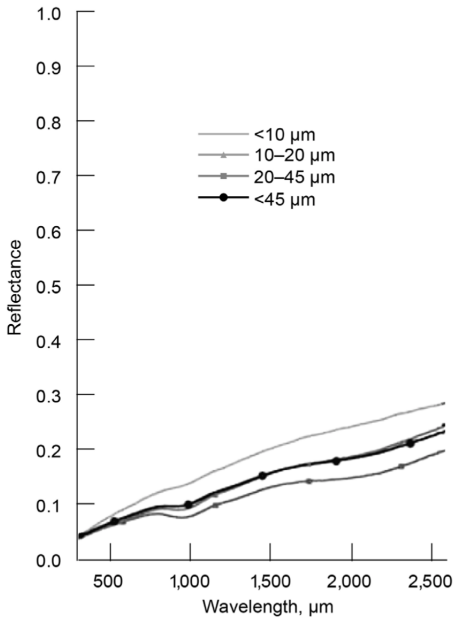

2.3 Summary

The information gathered though this research will prove vital in understanding the process of hydrogen reduction. Through the studies viewed throughout this chapter, an understanding on how the reduction temperature, pressure, and the sample's physical characteristics impact the reduction process has been established. This knowledge will be applied to the experiment that will be conducted and analysed later in this thesis. In addition to this, based of these studies the reduction temperatures implemented within this study shall be 600°C, 800°C and 1000°C, temperature which both incite reduction and minimise effects such as sintering and clumping. The reduction pressure shall also remain at 1atm, as demonstrated in figure 2.3 pressure has little effect on the conversion of iron oxide in this temperature range. Moreover, figure 2.2 demonstrates how the temperature has a greater effect on the conversion rate during hydrogen reduction. As such, the temperature shall be the only changing variable as this will provide greater difference

in reduction in durations of 2 hours and 4 hours.

With regards to the optical spectra analysis that has currently been conducted on in-situ lunar samples, extracted lunar samples, and lunar simulants, this state of the art has provided detailed summaries of these study's findings, which has revealed information that will be essential in the analysis of the simulant's optical spectra which will later be produced from this thesis. One of these major characteristic is how the lunar simulant JSC-1 produces a reflectance spectrum similar to that of the lunar mare, allowing the results produced by this study to be seen as a relevant reference for when analysing in-situ lunar mare spectra. Conversely, it was seen that FJS-1 differs in reflectance compared to that of the Apollo 12001 mare sample. This does not definitively mean that FJS-1's spectra can not be used as a reference for lunar mare analysis, as the Apollo 12001 sample does not represent the characteristics of the lunar mare in its entirety. Regardless, the ilmenite in FJS-3 provides an opportunity to view how this presence effects the reflectance produced within the UV wavelengths.

Evidently, Hapke's ratiative model offers a relatively accurate method to compute the abundance of SMFe for a given lunar sample. However, this model only utilises the relfectance of the sample in the visable and near infrared spectrum, disregarding the reflectance of the sample in the UV spectrum. This was nearly addressed in [15], however the aim of this study was to view the thermal reflectance of lunar dust as these particles will most likely not get filtered and contaminate lunar equipment. Therefore, this thesis will utilise the knowledge gained from the previous hydrogen reduction experiments, the maturity analysis conducted through [24, 25, 15], and other studies to replicate space weathering product and to evaluate the their corresponding reflectance spectra.

Chapter 3

Theoretical Discussion

This chapter aims is to discuss detail the concepts that were briefly mentioned in the previous chapter. This includes, discussing space weathering – the types of interactions that occur on the lunar surface, and the impact that it has on the lunar soil. Furthering this, the engineering properties of the lunar regolith will be discussed, utilising books like the ”The Lunar Sourcebook”, where a detailed analysis has been conducted on the Apollo mission samples [29]. A comparison will then be formed between the lunar simulants JSC-1 and FJS-3 - the simulant that will be analysed in this thesis, and the physical properties of the lunar samples. Once this comparison is completed, remote sensing and how it will be essential to explore the lunar surface, both efficiently and safely, for SMFe. In addition to this, both how remote sensing works and defining a wavelength which holds the potential to better extract SMFe from obtain spectra shall be discussed. In regards to the experiments that will be conducted in this thesis, a brief introduction to both hydrogen reduction, electron microscopy – specifying this further to scanned electron microscopy. This will see that aspects of these procedures that will later be conducted in this thesis is defined.

3.1 Space Weathering

Space weathering creates a dynamic environment where the lunar regolith is constantly changing both microstructurally and chemically. This has been backed up by many experiments and research conducted on the lunar samples gained from the Apollo missions. Ultimately, determining that the space weathering processes modifies the surfaces of the lunar soil grains [30], by analysing these modifications a consensus has been formed describing the type of weathering interactions present on the Moon. One of these processes is the impacting of micrometeorites which are seen as episodic heat events subsequently generating melting, vaporisation, and the dispersion of substrates [31]. Furthermore, along with the presence of solar winds both the microstructure and chemical composition of the lunar regolith changes. Solar winds are composed of ions and electrons, expelled from the Sun. More specifically, these solar winds consist of mostly protons, small amounts of double ionised helium, and traces of heavier ions [32]. Where these low mass ions such as hydrogen and helium are implanted, in high concentrations, to the lunar materials exposed to the Sun. Heavier ions, on the other hand, damage the lunar materials and leave latent tracks [33]. In this case, these are the only two space weathering interactions that will be taken into account.

With the space weathering processes being described, an understanding of how these interactions impact the lunar regolith microstructurally and chemically can begin. As previously stated, space weathering effects can be seen on the surface of lunar soil

grains. These visibly noticeable changes are known as rims and are assigned to 4 categories, based off of its microstructure and chemical composition [30]:

- **Amorphous Rims** - These consist of noncrystalline, a lack of crystalline structures and demonstrate a unique chemical signature corresponding to that of irradiation erosion. Confirming this, it has been demonstrated that exposing minerals to high flux, low energy ions (similar to that of solar winds) generate amorphous rims [34].
- **Inclusion-Rich Rims** - These are characterised by the abundance of nanometer-sized grains of Fe which are randomly dispersed in the layers of amorphous and silica rich matrix. On top of this, the chemistry consists with that formed from the settling of impact induced vapor i.e. the vapor generated from the vaporisation of regolith via micrometeorite impacts. This is evident from the distinct difference in its composition from the host grain.
- **Multiple-Rims** - Characterised by layers of rims distinct from one another by their microstructure and chemical composition. The inner layers tend to be damaged by radiation induced from solar winds, and coated by a layer formed from deposited impact-vapor.
- **Vesicular Rims** - This rim is chemically similar to its host grain, and characterised by an abundance of small vesicles, with diameters of ¡50nm. These vesicles occur in a 100nm layer surrounding the grain and are thought to be produced from the development of embedded solar-wind gasses during a pulse-heating event.

Seen above is the descriptions of how space weathering impacts the structure and the types of structures which are formed from space weathering events, but how do these processes chemically affect the regolith? As previously stated, due to the solar winds H+ ions are embedded into the lunar soil, acting as a reducing agent when the soil is melted and/or vaporised via micrometeorite impacts. When this occurs the the FeO is liberated, where the H+ ions act as the reducing agent, subsequently resulting in the production of npFe^0 [35]. This process corresponds to the formation of amorphous rims on lunar soil grains. It must also be stated that experiments utilising solely helium ions have produced nanophase iron without the addition of embedded hydrogen ions [36].

This is not the only process that contributes to the formation of nanophase iron particles. Evidence is given for this by amorphous rims forming on plagioclase grains, where nanophase iron particles are not native [35]. Thus, the reaction displayed in equation 3.3 is not the only reaction taking place on the surface of the Moon. In 1975 Hapke, et al. [22] proposed a method which also generates reduce nanophase iron particles, at first support was hard to come by with a lack of evidence, but later this changed through the discovery of vapor-deposited rims [30]. The method proposed that ion radiation generates sputtering and redeposits material on the surrounding lunar soil grains. In this case, oxygen is preferentially sputtered generating a reducing environment on the surface of the particles. Due to the low sticking coefficient of oxygen, the oxygen is lost from the system, thus reduced iron is found on the residual materials. Conversely, if cations are sputtered, they stick to adjacent grains generating a reducing environment on the target material, subsequently reducing the redeposited iron [35].

Additionally, a proposed method of iron reduction forming solely due to micrometeorite impacts has also been established. This however has yet to be supported due to the fact that this process relies on vapor condensing onto the surrounding glassy matrix. Yet agglutinate grains seen on the Moon are determined to be formed from the condensation

of melted substrates not from vaporised materials. Nevertheless, this process shall be looked at as it reveals an interesting behaviour of the oxides present in the lunar surface. Thus, proposed was that when a micrometeorite impact, the oxides like SiO, MgO and FeO vaporise. FeO has been found to posses the lowest binding energy out of these oxides and therefore the two elements separate. Due to oxygen's volatile state (low sticking coefficient) it stays in the vapor, whilst the, now metallic iron, condenses and forms in the surrounding materials [35].

With the chemical impacts, directly contributed from the interactions of space weathering now discussed it can be seen that the space weathering seems to only produce metallic iron. This does not account for the reason why in lunar samples iron is seen to be in an oxide form not its metallic form. Hence, another process is occurring which is subsequently oxidising the iron in the lunar regolith. The oxidation of nanophase iron particles is an area which has been researched into great depth, revealing that metallic iron does not need to be directly exposed to an atmosphere but can oxidise even when covered by a substrate. A characteristic due to the nanopahse particle's large surface area [35]. This proves that nanophase iron particle can reduce in an atmospheric vacant environment, but does this occur in the low temperatures on the Moon. In fact, oxidisation can take place in relatively low temperatures proven by the formation of an oxidised film in temperatures $<$100K [37].

To conclude this section, it has been proven that the environment present on the lunar surface is a dynamic place, where the microstructure and chemical composition of the surface grains is constantly changing. Forming metallic iron due to the highly reductive environment present from the many space weathering interactions. In addition to this, the products from the reductive environment, the npFe^0, oxidises back to the original oxidised iron previous to the reduction due to the high surface area. It is also evident that the products of space weathering all occur on the surface grains present in the lunar surface - a factor that will be taken into account when discussing the wavelength used to generate the optical spectra later in this thesis. Finally, through the study of the space weathering events it is clear that hydrogen in the key reducing agent present on the surface of the Moon, furthering backing up the selection of implementing hydrogen at the reducing agent utilised in this study's experiments.

3.2 Properties of Lunar Regolith

The properties of the lunar regolith discussed in this section will consist of the geotechnical and engineering properties. These factors are essential to understand the behaviour of the lunar regolith. Stated in the previous chapter the factors which impact the products of the hydrogen reduction process was defined. Therefore, these are the areas that must be taken into account when viewing the characteristics of the lunar regolith and subsequently the lunar simulants JSC-1 and FJS-3. In addition to this, the factors that may impact the optical spectra generated by the lunar simulants JSC-1 and FJS-3 shall be discussed. This section provides the basis for the comparison of the lunar regolith and lunar simulants JSC-1 and FJS-3.

Stated in the previous section, micrometeorite impacts are a frequent occurrence, generating a dynamic environment on the lunar surface. Consequently, the lunar soil has reached a "steady state", in terms of it's geotechnical properties [29], and with the lack of diverse weathering effects, as oppose to that on Earth, these parameters are in a narrow range. Nevertheless, variables such as particle size distribution, particle shape,

specific gravity, bulk density and porosity of the lunar soil shall be discussed and how these characteristics impact the behaviour of the lunar soils. Discussing these provides a range a parameters to compare to the lunar simulants JSC-1 and FJS-3.

3.2.1 Particle size distribution

Stated before due to impacts from micrometeorites and the lack of erosion type weathering such as winds and rain the particle sizes of the lunar regolith are determined to be in a narrow range. It must also be said that for unconsolidated materials, i.e. soils, the particle size distribution influences the strength and compressibility of the material [29]. Statistical definitions such as the mean, median, standard deviation, skewness and kurtosis can be used to better define the particle size distribution of the soil. Nevertheless provided through [38] the mean sizes of the Apollo samples are acquired (refer to table 3.1).

Table 3.1: Mean size of lunar samples acquired from [29], where [38] was referenced.

	Mean size	
Soil ID	**$<$1cm (μm)**	**$<$1mm (μm)**
10002	-	52
12001	-	60
14003	129	99
14141	616	123
14163	76	56
15220	-	43
15270	-	94
15400	330	61
61180	94	64
61220	216	68
62280	134	70
64500	104	65
68500	106	68
70180	67	58
71500	83	65
72140	57	50
72500	67	57
73240	127	51
74220	-	41
78220	50	45
78500	46	41

3.2.2 Particle shape

Whereas the size distribution has a fairly narrow range, demonstrated through table 3.1 the shape of the lunar soil can vary ranging from being spherical to extremely angular. Although in general, particles tend to be elongated and range from sub-angular to angular, demonstrated in table 3.2. The particle's shape is fully defined by the following measurements must be made [29]:

- **Elongation** - The ratio of the major and minor axes of the particle.
- **Aspect Ratio** - The ratio between the minor and major axes of the particle

- **Roundness** - The ratio of the average radii to the corners of the particle and the radius of the maximum inscribed circle.
- **Volume Coefficient** - The volume of a particle divided by the cube of the diameter of a circle which encloses the same area as the particle profile.
- **Specific Surface Area** - The surface area of a particle divided by its mass.

Determined from various analysis on lunar samples an average of each of these parameters has been formed by measuring many lunar particles. These average values are displayed below:

Table 3.2: Average shape of lunar particles. All references retrieved from [29].

Parameter	Average Value	Reference
Elongation	1.35	[39]
Aspect Ratio	0.55	[40, 41]
Roundness	0.22	[42]
Volume Coefficient	0.3	[39]
Specific Surface Area	0.5 m^2/g	[43]]

3.2.3 Specific Gravity

The specific gravity is defined as the ratio between the mass of the particle and the mass of an equal volume of water. The parameter is measured by submerging a material into a fluid. This method fills two types of porosities, the intergranular and intragranular which characterises the space around the exterior of the particles. The interior space, also known as the subgranular porosity, remains unaffected and thus reduces the measured specific gravity [29]. These types of porosities will be later defined. Tests conducted in 1970 have measured the specific gravity of soils finding the results displayed in table 3.3. Provided in the Lunar Sourcebook, a recommended value of 3.1 is proposed for scientific and engineering analysis purposes [29].

Table 3.3: Specific gravity of soil types which are present on the Lunar surface [29].

Agglutinate and glass particles	1.0 to $>$3.32
Basalt particles	$>$3.32
Breccia particles	2.9 to 3.10

3.2.4 Bulk Density

Bulk density is defined as the mass of a material in a given volume (refer to equation 3.1)

$$\rho = G\rho_w(1-n) \tag{3.1}$$

where: ρ is the bulk density, G is the specific gravity, ρ_w is the density of water and n is the porosity of the material.

The bulk density has an influential role on the materials bearing capacity, slope stability, seismic velocity, thermal conductivity, electrical resistivity and depth of penetration of radiation [29]. Also given in the Lunar Sourcebook is the average bulk densities of the soil, relative to their depth. This data was produced through various forms of analysis

conducted over the years of lunar exploration. These techniques include: remote sensing, using infrared spectrometry to gain an early estimation of the lunar particles bulk density; Robotic measurements, gained from the Surveyor, Luna and Lunokhod mission - inferred data based off of lunar soil simulations aided with analysing the images taken of boot prints and track prints left by the astronauts on the Moon, and finally the analysis of returned lunar samples [29]. Taking into consideration of all of the analytical techniques, an average value of the lunar soil particles bulk density has been deduced (refer to table 3.4).

Table 3.4: Average Bulk Density of Lunar soil [29].

Average Bulk Density (g/cm^3)	**Depth range** (cm)
1.50 $\pm$ 0.05	0 - 15
1.58 $\pm$ 0.05	0 - 30
1.74 $\pm$ 0.05	30 - 60
1.66 $\pm$ 0.05	0 - 60

3.2.5 Porosity

Defined as the volume space between the particles divided by the total volume of the material. The porosity can be divided into three categories [29]:

- **Intergranular Porosity** - The volume of space between the individual particles.
- **Intragranular Porosity** - The volume of space in the re-entrant surfaces on the exterior of the particles.
- **Subgrannular Porosity** - The volume of enclosed spaces within the interior of the particle.

The porosity can also be furthered defined in terms of the void ratio. Where the void ratio is defined as the ratio of the void space between the particles and the volume of solid particles (refer to equation 3.2).

$$e = \frac{n}{1-n} \tag{3.2}$$

Where: e is the void ratio and n is the porosity.

3.2.6 Relative Density

Relative density is an important variable which defines the assembly of a material, where it takes into account the arrangement of particles. For example, assuming the particles are spherical, the packing arrangement of these particles can be in a square packing arrangement. In other words drawing a line through four adjacent spheres a square is formed. This packing order can be considered to be the loosest, as the there is maximum void space (refer to figure 3.1a). On the other hand, the opposite extreme is that the particles packing order forms a hexagonal packing where the void space is at its minimum (refer to figure 3.1b).

Figure 3.1: 3.1a: Square Packing arrangement. 3.1b: Hexagonal Packing Arrangement [44].

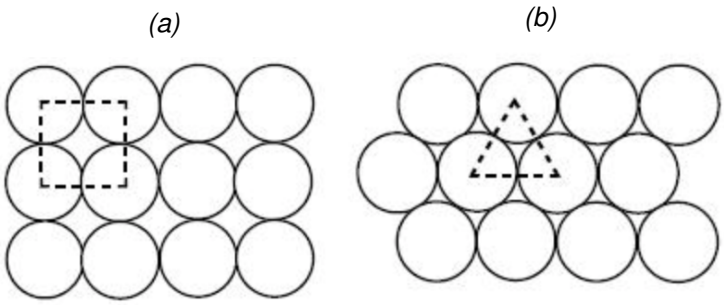

3.2.7 Composition

To finalise this study of the lunar soil, the chemistry of the samples gained from both the Apollo missions and Luna missions must be defined. The composition of the site locations in which these missions landed at can be viewed in table 3.5.

Table 3.5: NASA Data (1982) gathered from the Data Base Compilation of the Lunar Sample Curator, NASA Johnson Space Center, Houston, TX [45].

	Mare									
	High Ti		Low Ti			Highlands		Basin Ejecta		
Oxides	**A-11**	**A-17**	**A-12**	**A-15**	**L-16**	**A-16**	**L-20**	**A-14**	**A-15**	**A-17**
Al_2O_3 (wt%)	13.78	10.97	13.71	10.32	15.51	27.18	23.07	17.41	17.54	20.6
CaO (wt%)	12.12	10.62	10.55	9.74	12.07	15.79	14.07	10.79	11.57	12.86
Cr_2O_3 (wt%)	0.3	0.46	0.35	0.53	0.29	0.107	0.15	0.22	0.28	0.26
FeO (wt%)	15.76	17.53	15.41	19.75	16.41	5.18	7.35	10.36	11.58	8.59
K_2O (wt%)	0.15	0.076	0.27	0.1	0.1	0.11	0.08	0.58	0.17	0.16
MgO (wt%)	8.17	9.62	9.91	11.29	8.79	5.84	9.26	9.47	10.41	10.29
MnO (wt%)	0.21	0.24	0.22	0.25	0.21	0.065	0.11	0.14	0.16	0.11
Na_2O (wt%)	0.44	0.35	0.48	0.31	0.36	0.47	0.35	0.7	0.42	0.41
P_2O_5 (wt%)	0.12	0.07	0.31	0.11	0.14	0.12	0.11	0.5	0.16	0.14
SiO_2 (wt%)	42.17	39.87	46.17	46.2	43.96	45.09	44.95	48.08	46.59	45.08
TiO_2 (wt%)	7.67	9.42	3.07	2.16	3.53	0.56	0.49	1.7	1.32	1.62

It is evident through table 3.5 that the locations in which display the highest quantities of iron oxide is that of the mare and basin ejecta. In terms of the formation of these areas and why they contain larger quantities of iron oxide is considered to be out of this projects scope. Therefore, these aspects shall not be elaborated upon.

3.3 A Comparison between Lunar Simulants JSC-1 and FJS-3 to In-Situ Lunar Samples

The previous section describes the properties of the lunar regolith based off of the samples returned from the Apollo missions. Building upon this, a comparison will be made to evaluate the similarities that JSC-1 and FJS-3 to that of the lunar samples. This sections aim is to analyse both lunar simulants JSC-1 and FJS-3 and give reasons to why these simulants will be utilised in this study. This analysis will demonstrate that if the same study, which will be carried out in this thesis, was conducted on a lunar sample the results would be somewhat coherent.

3.3.1 Lunar Simulant JSC-1

Lunar simulant JSC-1 has been a widely used simulant, developed and characterised by NASA, Johnson Space Center, hence the abbreviation "JSC". Derived from volcanic ash, composed chemically of basalt, it was produced to mimic that of the soil gained from the lunar mare regions. As such it was produced so that its chemical composition, mineralogy, particle size distribution, specific gravity, angle of internal friction, and cohesion all fall within the range of the analysed lunar mare samples [46]. Displayed below is the bulk Chemical composition of the JSC-1 simulant (refer to table 3.6).

Table 3.6: Bulk chemical composition of lunar simulant JSC-1 and Apollo 14 samples.

Oxide	**wt% of JSC-1** [46]	**wt% of Apollo 14 samples**
SiO_2	47.71	48.08
TiO_2	1.59	1.7
Al_2O_3	15.02	17.41
Fe_2O_3	3.44	-
FeO	7.35	10.36
MgO	9.01	9.47
CaO	10.42	10.79
Na_2O	2.70	0.7
K_2O	0.82	0.58
MnO	0.18	0.14
Cr_2O_3	0.04	0.22
P_2O_5	0.66	0.5
LOI	0.71	-

By viewing the bulk chemistry of lunar simulant JSC-1, there is a clear similarity to the basin ejecta found from the Apollo 14 mission. However, it must be stated that there are compounds that appear that appear in the composition of JSC-1 which do not appear in lunar samples. For instance, the compound Fe_2O_3, also known as hematite, has only been recently found in soils at high altitudes [47]. Nevertheless, Hematite represents Fe^{+3}, an oxidisation state which on the Moon is extremely uncommon. Due to the extreme reducing environment that is present on the surface of the Moon, which has been described above, hematite is an uncommon oxide. Moreover, as lunar simulant JSC-1 was developed to simulate the lunar mare, where hematite has yet to be found, this study and the appearance of hematite shall be disregarded.

LOI, better known as the loss on ignition, constitutes to the water, sulfur and chlorine

compound contents which appears in the lunar simulant. As the weight percentage of this component is relatively small, it will not have a major impact on this study. Although, it does pose the opportunity for discussion that lunar samples gained from lunar missions have yet to contain these volatiles. As such, in order to remove the majority of these substances the simulant was heated at 900°C for an hour in argon [46].

Mineralogy

The contents of JSC-1 are recorded to consist of crystolline phases such as plagioclase, pyroxene and olivine, with trace of ilmenite and chromite [46]. All of which are consistent with that of the lunar mare soils. However, lunar simulants contain large quantities of agglutinate glass, a substance which is produced through the various space weathering interactions, a product of the cooling of impact-vapor. Although glass structures do appear in JSC-1 there is a no nanophase iron particles within the glass. As oppose to what appears in the agglutinate glass structure in the lunar soils. The volcanic glass that appears in JSC-1 in fact contains more micrometer-scale plagioclase and metal crystal oxides when compared to the lunar samples [46].

Specific Gravity

Displayed in [46], the specific gravity of JSC-1 is 2.9g/cm^3, which is consistent with the recorded specific gravity's displayed in table 3.3. The specific gravity of JSC-1 was measured by computing the ratio of the particle mass to the mass of water which has an equal volume measurement at 4 $^{\circ}$C.

Particle Description

Consistent with the submature lunar sample [46] as the particle size distribution of JSC-1 falls within this range, with a mean range of 102 μm, although, it has a narrower particle size range, oppose to most lunar samples.

With regards to the particle shape of JSC-1, explicit information stating this characteristic was not found in [46]. However, a study analysing the 3D shape of JSC-1A has been completed [48], where the spherical harmonic series is implemented. JSC-1A is a simulant based off of JSC-1 and posses almost identical characteristics and thus using this study will reveal an indication on some of JSC-1's particle shape characteristics. In this analysis cumulative curves describe the JSC-1A's surface area and aspect ratio. Thus only a range where most of the particles fall into can be determined. Therefore, the surface area of JSC-1A falls between 0.1 - 1.3 mm^2, whereas the aspect ratio (ratio between the particles length and width) is determined to be between 1 and 2. In order to make a valid comparison between the surface area described here and the values displayed in table 3.2, the surface area would need to be divided by the samples mass, as the value provided in table 3.2 is that of specific surface area. A comparison however can be made between the aspect ratio, defined here and that seen in table 3.2. As the aspect ratio is heavily influenced by what is considered as the particles length and the particles width i.e. it is defined by the viewer, it is reasonable to assume that the aspect ratio recorded here is that of the elongation recorded in table 3.2. Taking this into account the elongation in table 3.2 falls within the range determined from [48]. Further study will need to go into this to determine the further particle shape characteristics of JSC-1. In general however, the particles demonstrate sub-angular to angular characteristics [46], a definition which has been previously used to define the characteristics of the lunar samples.

Summary

It must be stated, with all the similarities that have been made between the lunar mare soil and simulant JSC-1 there is one characteristic that cannot be replicated precisely. This is the agglutinate glass that binds the rock and minerals together in the lunar soil. This glass is formed from high impact and extremely reductive environment that is present on the surface of the Moon. These conditions have yet to be effectively simulated in laboratories and as such this is an aspect that can not easily be replicated. For this reason, further study will be need to be on in-situ samples in order to fully understand what a substance, such as agglutinate glass, will have on the production of metallic iron through hydrogen reduction.

3.3.2 Lunar Simulant FJS-3

The FJS simulants were developed by the Shimizu Corp., a Japanese based corporation, where three types of simulants were created, FJS 1,2 and 3. All of which are based off of volcanic basalt from Mt. Fuji [49]. The differences begin where FJS-1 is 100% basalt, FJS-2 has a spike of oviline and FJS-3 is spiked with both oviline and ilmenite. It must be said, that there is very limited information with regards to the FJS simulants and even less when specifically searching for FJS-3. Taking this into account, this comparison will be viewing information that describes FJS-1, as no information has been found that reveals a significant difference between the simulants FJS-1 and FJS-3, except for their bulk chemical compositions.

Table 3.7: Bulk chemical composition of lunar simulant FJS-3 [50] and bulk chemistry of its closest equivalent from table 3.5.

Oxide	wt%	A-12 wt%
SiO_2	46.0	46.17
TiO_2	6.7	3.07
Al_2O_3	13.7	13.71
FeO	7.9	15.41
Fe_2O_3	5.9	-
MnO	0.28	0.22
MgO	7.3	9.91
CaO	7.8	9.74
Na_2O	2.6	0.48
K_2O	0.87	0.27
P_2O_5	0.39	0.31
H_2O	0.58	-

Mentioned above, FJS-3 is composed of basalt (81%), oviline (11%) and ilmenite (8%), three minerals that are known substances within the lunar regolith. With further definition to the bulk chemical composition of FJS-3, it is clear that FJS-3 is a simulant replicating that of the lunar maria composition. By referring to table 3.7 the closest similarity between FJS-3 and the Apollo and Luna samples is with A-12 (the sample gained from the Apollo 12 mission. Evidently, the composition of FJS-3 is similar to that of the lunar simulant JSC-1, although has a substantially larger percentage of titanium dioxide, accounting for the greater spike of ilmenite.

Studies have been conducted in order to analyse the shape characteristics of FJS-1 [51], by implementing the discrete elemental method (DEM). Through this study an aver-

age value for the particles elongation is determined to be 0.723, this value was based off of X-ray CT scans and gathered an average after measuring $>$1000 grains. The elongation determined through this study, again displays similarity to the aspect ratio provided in table 3.2. Thus, it can be said that these grains have a similar aspect ratio to that of the lunar samples. As aspect ratio can be determined by the inverse of the particles elongation. This characteristic can be compared to JSC-1, resulting in the aspect ration of FJS-1 being in the lower range of that determined from studying JSC-1.

Further study will need to go into determining the physical characteristics of FJS-3. This might be difficult however, as the simulant is no longer produced. Nevertheless, with the quantity that has already been produced, and the proportion being viewed in this study, analysing FJS-3 will provide some additional clarity to this simulant.

3.4 Remote Sensing and how it will aid in Exploring the Lunar Surface

Remote sensing offers a unique way to explore the surface of the Moon. Being able to analyse the lunar surface from orbit will considerably decrease the cost of locating in-situ resources, as the need for rovers or manned expeditions will be redundant in this phase of exploration. As an example, the Moon Mineralogy Mapper (M^3), which was aboard the Chandrayaan-1 [4]. The M^3 is an image spectrometer which orbits the Moon [52]. This one spectrometer has the ability to scan 25% - 50% of the surface of the Moon [4], a proportion which would take many expeditions to even come close. In addition to this, remote sensing offers the chance to view the Moon's surface in its natural state. Although samples have been gained through lunar expeditions, these samples required to be dug, potentially disrupting the surface layer of the lunar regolith [14]. Consequently, meaning that lunar simulants are referenced to samples that do not fully represent the lunar soil and its untouched form. A factor which was briefly discussed in the previous chapter, but with no definitive answer. Therefore, this section shall explore remote sensing, determining how this technique delivers information that will prove essential in the exploration of the Moon for SMFe.

Just like how our eyes work, in the sense of receiving visible light waves that have been reflected off an observed object, remote sensing has the capability to detect light in a variety of wavelengths. This essentially provides the viewer with a new pair of eyes, and a completely different view of an object. The stages of remote sensing can be broken down into the following [53]:

- Emission of electromagnetic waves.
- Absorption, reflection and scattering of waves interacting with the observed object.
- Detector interacting with the reflected electromagnetic waves.
- Sensor outputs data.
- Data is then transmitted, processed and analysed.

This study will utilise remote sensing within the ultra violet (UV) spectrum. Due to UV's short wavelength and subsequently high energy, UV penetrates a substance far less. This behaviour is something that goes hand-in-hand when evaluating the lunar surface for SMFe. Stated above, metallic iron produced from space weathering predominately

appears in the amorphous rims i.e. the surface of the lunar grains. Hence, in theory the shorter wavelengths of UV light will interact far greater with the amorphous rims present in the lunar soil. As an example, in [54] it is stated that "the spectral reflectance of lunar soils in short wavelengths is less sensitive to the variation of the host grains reflectance, while being mainly controlled by the variation of npFe^0 abundance". Backing up the theory that UV will interact far greater with the npFe^0 as oppose to other wavelengths. For the purpose of this study UV-VIS shall be implemented, utilising the spectra to form the preliminary basis for viewing the effects due to the presence of SMFe, which later after denser quantities of data is retrieved a comparison can be formed between the spectra generated in the UV-VIS range and that of the spectra formed within the VIS-NIR range.

3.5 Hydrogen reduction

Hydrogen reduction is an extraction process which has been studied for many years. It demonstrates future methods of extracting metals from their ore state while simultaneously minimising the carbon dioxide emitted into the atmosphere here on Earth. On top of this, hydrogen reduction possesses the ability to obtain water, then through electrolysis oxygen is obtained from the lunar soil. Hydrogen is used as a reduction agent due to its extremely high reactivity, which provides the best possible chance for a solid-gas reaction to take place under a variety of physico-chemical conditions. Furthermore, described in equation 3.3 and the process of electrolysis, separating the hydrogen and oxygen present in the bi-product of the reduction. Theoretically, the hydrogen can therefore be recycled giving evidence of the possibility for a closed system. A potential which would ultimately reduce the cost of the extraction process and the required hydrogen needed for this process. This is an observation made through the research conducted in [9].

Nevertheless, this method is tried and tested in generating npFe^0 and SMFe, the main products of space weathering. By implementing this method it is possible to generate samples containing these space weathering products and as such provide the opportunity to view the impact of these products on the optical spectra of the lunar simulants. On top of this, transmission Mössbauer analysis shall take place, this will offer the ability to quantify the metallic iron produced via this reaction, both providing preliminary quantification for comparison of the optical spectra and presence of SMFe, but a preliminary value of the quantity of metallic iron generated for the specific test conditions applied.

$$FeO + H_2 = Fe + H_2O \tag{3.3}$$

Reduction is defined as the absorption of electrons and, respectively, the diminution of the oxidation state. In terms of metallurgic uses, reduction is indicated as the removal of oxygen from oxide and its conversion to an element or to the subordinated oxidation state [55]. Clearly seen in the chemical equation shown above 3.3. As FJS-3 contains quantities of ilmentite an understanding of its reaction must take place. This is demonstrated through equation 3.4.

$$FeTiO_3 + H_2 = Fe + TiO_2 + H_2O \tag{3.4}$$

The two reactions displayed in equations 3.3 and 3.4 are considered to be the only two reactions that are taking place during the hydrogen reduction process. Therefore the products generated from this reaction will be the only product taken into account when analysing the change in optical spectra. This assumption is formed after discussing in the previous chapter and sections that iron oxide holds the weakest chemical bond out of the substances present in the lunar simulants. With regards to ilmenite, this reaction

is heavily studied and also produces metallic iron therefore is also considered. It must be stated however, by considering equation 3.4 products not only the increase in metallic iron can be considered, but also the increasing presence of titanium dioxide (TiO_0).

3.6 Electron Microscopy

Microscopy is the study of objects that are too small to see with the naked eye. In this case, microscopy is a vital tool to analyse the physical shape and sizes of the lunar regolith, both before the reduction process and after. Electron microscopy utilises the wave like behavior that electrons exhibit. By accelerating the emitted electron (primary electrons), the electron's wavelength decreases to a size where diffraction occurs (refer to equation 3.5). This is known as transmission electron diffraction and first demonstrated for analytical purposes by Thomson and Reid in 1927 [56].

$$\lambda = \frac{h}{p} \tag{3.5}$$

Where: λ is the De Broglie wavelength, h is Plankk's constant and p is the particles momentum.

Electron microscopy was continuously developed through the 20th century, where not only different forms of electron microscopy was created, but the ability to develop high resolution images of the samples structure became a reality. On top of this, with the addition of devices it is possible to determine the chemical compositions of the specimen. This analytical method is possible due to the bombardment of the emitted electrons with the electrons existing in the specimen. When the energy transmitted in the collision is sufficient to increase the electrons quantum energy state (excitation), the electron will eventually lower to its original energy state (de-excite), emitting a photon with an energy equal to the difference of the two energy states. This fact is important due to every element and compound emitting unique photons from this interaction, and therefore can be identified.

3.6.1 Scanned Electron Microscopy

In this study SEM will predominately be used to analyse both the unprocessed and processed lunar simulants. Implementing techniques such as back scattering and secondary electron analysis, in order to gain a level of understanding of the reactions that have taken place during the hydrogen reduction phase. Therefore, for the remainder of this section SEM and the techniques just described shall be elaborated upon.

There are two general types of electron microscopy, transmission and scanned. Previously mention Scanned Electron Microscopy (SEM) will only be taken into consideration, so how is it defined? Well, oppose to Transmission Electron Microscopy (TEM), SEM utilises much lower voltages, this is so that the electrons do not actually penetrate the sample, but are reflected. This means that SEM's can produce high resolution imagery of the sample's topography. On top of this, an SEM also provides information about the samples composition [57]. For this reason, the SEM is the perfect tool to be implemented for the sample analysis in this study.

Briefly explained above is how SEM generates images detecting the emitted electrons close to the surface of the sample. The electrons emitted at different depths of the sample provide unique information about the sample. Through [57] the emitted electrons with a

Table 3.8: SEM components and their description [57].

Component	Description
Electron Column	This is where the electron beam is generated once a vacuum has been induced. The electron beam is directed and focused towards the sample by electromagnetic deflection coils.
Electron Gun	Electrons are emitted thermionically (the emission of electron from a very hot solid or liquid). Due to having the highest melting point of metals, one of the lowest vapor pressures and a relatively low cost, tungsten is the most widely used substance which is heated in an electron gun.
Condenser Lenses	Along with the selected accelerating voltage, the condenser lenses define the beam intensity. The beam passes through two condenser lenses, which converges the beam once it has passed the anode.
Apertures	The final lens aperture determines the diameter of the beam, ultimately controlling the resolution and depth of field viewed in the image. By decreasing the diameter of the beam size, both the resolution and depth of field increases in the produced in the image.
Scanning System	”Images are formed by rastering the electron beam across the specimen using deflection coils inside the objective lens. The stigmator or astigmatism corrector is located in the objective lens and uses a magnetic field in order to reduce aberrations of the electron beam”, ensuring a quality image is produced.
Specimen Chamber	Here is where the specimen is loacted, where the position of said specimen is controlled via a goniometer.
Electron Detectors	Detectors collect the signal generated from the interaction between the beam and the specimen. These detector convert the signals captured into a digital image which can then be analysed.

brief definition is provided. In this study however, only the backscattered and secondary electrons will be utilised, along with the characteristic X-rays to determine the sample composition. Therefore, these will be the only types of reflected energies that will be elaborated upon. Additionally, it can also be seen in [57] it is seen that the depth in which the incidence electron penetrates the sample correlates to the emitted energy released. Evidently, demonstrating a relationship between the incident electrons energy and the data collected.

Secondary Electrons (SE)

Compared to the BE, secondary electrons posses less energy, thus are unable to penetrate the majority of substances. For this reason, it provides a suitable method in producing imagery which displays the topography of a sample. Demonstrating images with a resolution power of 10nm. Just like BE a special detector is required to obtain SE imagery from an SEM.

Backscattered electrons (BE)

These electrons are considered to have high energies. Utilising a specific detectors which traps these electrons, it is possible to differentiate the sample imagery by the different atomic numbers which appear in the sample [57]. A visual difference is present in the BE images due to a substance's atomic number, as the denser a substance (the greater atomic number), the greater quantity of electrons are reflected and therefore the brighter it will appear in the images produced [58]. Proving to be a powerful tool which will aid in discovering a preliminary view of the nanophase iron within the sample prior to the spectroscopy analysis.

3.6.2 Characteristic X-rays

Mentioned above is the term energy states, by bombarding the electrons in an atom with an electron with a high enough energy, the bound electron can move to a higher energy state. Each atom has unique energy states, which require specific amounts of energy to enter the next energy state. When an electron moves down an energy state a high energy photon is emitted, in the form of an X-ray [57]. Hence why these emitted particles are named ”characteristic X-rays” because the unique photons emitted reveal information specifying the sample's composition.

Chapter 4

Development of the chosen solution

In this chapter, the experiments - elaborating upon the test conditions, along with the equipment that was implemented for the various experiments shall be discussed. These experiments aim to determine how the formation of SMFe impact the optical spectra generated via lunar simulants JSC-1 and FJS-3. Therefore these simulants will be analysed both unprocessed and processed in order to produce data which can be effectively compared. To conclude this chapter, the experimental risks must be defined, this was written both before an after the experiments were completed. This is due to the fact that the areas in which were predicted to cause an contamination or any other risks can be backed up by evidence from the experimental results.

4.1 Experimental Procedure

Previously discussed in this study is the dynamic environment that occurs on the lunar surface. A known and common interaction is the embedding of light ions emitted via the Sun (e.g. Hydrogen and Helium), known as solar winds and the impact of micrometeorites which generate momentary heat events. Consequently melting and vaporising the lunar regolith by generating a suitable environment to reduce the oxides present in the lunar soil. In order to simulate this environment the lunar samples JSC-1 and FJS-3 will reduced via a hydrogen flow placing through samples tested at 600°C, 800°C and 1000°C. From the studies which have been discussed with chapter 2 all of these temperatures are known to incite the reduction iron oxide. These tests will first be ran for 2 hours and then 4 hours, this is accomplished to verify if the reduction duration has a noticeable effect on the on the production of SMFe.

Once reduction is completed, the samples shall be analysed via an SEM. As previously mentioned both secondary and backscattered electrons shall be utilised to view the samples topography and located any denser atomic weights which may represent the formation of metallic iron. The chemical composition of the samples will be evaluated via a software which identifies the atomic weight of the location deem of interest. By viewing the chemical composition of various sites of interest within the produced samples, confirmation on the production of SMFe can be achieved. In addition to this, the sizing of these SMFe is achievable due to the microscopes definition of a scale, allowing for the comparison of metallic iron particle sizes between each of the samples to be possible, This will aid in the analysis of the corresponding optical spectra, as it was previously mentioned through the research conducted in chapter 2 the sizing of the metallic iron holds great effect on the darkening and reddening of the spectra in question.

Optical spectra shall be obtained through the wavelength range of 200nm - 800nm, evidently spanning through the UV-VIS spectrum. When discussing remote sensing in the previous chapter, the potential of UV wavelengths to detect space weathering produced metallic iron was established. In addition to this, Hapke's radiative model only considers wavelengths in the visible and near-infrared region. For this reason, it is determined that obtaining the sample's reflectance in the UV region and attempting to quantify the changing optical properties of the sample with increasing presence of SMFe is essential to eventually compare the accuracy of a UV model to Hapke's radiative model.

To conclude the experimental procedure a Transmission Mössbauer analysis shall be conducted. The data which will be obtained through this will generated a preliminary view of the production iron. Establishing the basses to quantify the metallic iron content within the processed sample. To effectively complete this analysis the unprocessed sample and a processed sample will need to be tested. The selection of the simulant and the specific sample will occur later in this study. This is to allow for the characterisation via SEM to be completed, therefore an informed selection process can occur.

4.2 Experimental Equipment

4.2.1 Hydrogen Reduction

The reactor tube housing the lunar simulant samples was a stainless steel reactor tube, this reactor has an internal diameter of 4mm. To ensuring that the sample does not escape from the reactor tube quartz wool was employed. Quartz wool is an organic substance that will not react with the sample whilst exposed to high temperatures. In order to heat the sample to the required temperatures a Carbolite furnace, model MTF 12/38/400. Utilising the ramp setting, the user can adjust the rate of temperature increase, for this study the setting implemented was 40°C/min. Setting the dwell time determines how long the sample will be exposed to the desired temperature, in this case the two dwell times selected are 2 hours and 4 hours. To aid the furnace and minimise the energy needed to heat the reactor chamber to the desired reduction temperature, fabric insulators are wrapped either end of the reaction chamber. This reduces the amount of heat escaping the system, subsequently increasing the efficiency of the furnace. To analyse the hydrogen flow a Bronkhorst mass flow controller was utilised. Not only does this equipment measure the hydrogen flow, but allows the user to adjust the flow to the required amount.

4.2.2 SEM

Housed at the Universitat de Politecnica de Catalunya, EEBE campus, is a Field Emission Scanning Electron Microscope (FESEM) which was utilised for this phase of the experiment. In order to initialise this phase, the samples require preparation, involving coating the sample in carbon, via evaporation. Carbon increases the sample's conductivity, subsequently improving the images formed from the SEM. Once coated, a double sided adhesive tab, made from silicon is placed on an aluminium sample mount. The adhesive tab is required to ensures that when the vacuum is formed within the chamber, the sample is not removed from the sample mount, damaging the machine. To be certain that all of the placed sample is confined onto the adhesive tab, the sample is blasted with argon. Argon is a noble gas and as such will not react with the sample, this would compromising the analysis.

The detector implemented within this instrument consists of an Energy-Dispersive X-ray Spectroscopy (EDS), this detects X-rays and works in tandem with the INCA software [59] to generate energy spectra corresponding to the site of interests elemental composition. Additionally, the instrument is equipped with an BSE and SE detector to detect the backscattered and secondary electrons. With this set up, all the necessary images to accomplish the characterisation of the lunar simulant samples is possible.

4.2.3 UV - VIS Analysis

With the characterisation of each sample complete, the optical analysis shall take place. Utilising the Shimadzu UV-VIS-NIR Spectrophotometer (UV-3600), the sample's optical reflectance spectra shall be acquired in the ultraviolet (UV) and visible (VIS) region of the spectrum. As such the source of light for this analysis is a halogen bulb due to their emittance of UV and VIS wavelengths. To accurately quantify the wavelength which is being exposed to the sample, a diffraction grating is employed. On top of this a wavelength must be selected to define when the position of the light source will change, this is selected to be at 290nm. It must be stated that the range which can be selected is 282nm - 393nm [60], illustrating that the possible range is all within the UV region. It was therefore deemed that 290nm was the best suited wavelength for the light source position to change.

Table 4.1 demonstrates the three possible detectors which are present within the UV-3600. As this study is only utilising UV and VIS wavelengths, more specifically the range of 200nm - 800nm. Therefore to minimise the amount of noise generated, the PMT detector shall be employed. Within the chamber, Barium sulfate coats the interior. Barium sulfate is an extremely good reflector of UV and visible light, as such it is a suitable surrounding substance to the sample when measuring the reflectance.

Table 4.1: Detectors within the UV-3600 and their corresponding detectable wavelength range [60].

Detector	Wavelength range
PMT	165nm - 1,000nm
InGaAs	700nm - 1,800nm
PbS	1600nm - 3,300nm

4.2.4 Mossbauer Analysis

Based off of the preliminary characterisation of the sample during the SEM phase. A sample shall be selected to undertake the Mossbauer analysis, quantification of the amount of metallic iron produced is possible through this analysis. Therefore, an understanding on the correlation between the quantity of metallic iron and the optical properties of the lunar simulant can be formed.

The mössbauer technique relies on the formation of a magnetic field within the nucleus of the measured element. A when exposed to the gamma radiation emitted via the source, in this case cobalt 57, energy states shall form. These energy states, like the ones mentioned in the theoretical discussion are unique to an element and thus reveal the composition within a tested sample. The emitted radiation from the cobalt 57 has only one specific amount of energy. Therefore, the source is moved in the positive and negative direction, positive being defined as moving closer to the tested sample and

negative being the sample is moved in the opposite direction. With the source moving, the energy of the emitted particles vary due to the wavelengths experiencing blue and red shift. The velocity of the source is measured and scaled to a non-dimensional unit, known as channels, in a range of 0 - 400 channels. For this reason calibration of the system is needed in order to locate each absorption peak. The aim of this analysis is to quantify metallic iron, subsequently metallic iron is used for the calibration. Metallic iron posses six unique peaks, through this calibration the channels corresponding to each of these absorption peaks will be known. Through this all forms of iron will be quantitatively known in the lunar sample analysed.

This experiment was conducted at room temperature and pressure, with the sample being moved in a velocity range of $\pm$11.4m/s. To fit the spectra generated, the Brand NORMOS program was implemented.

4.3 Experimental Risk

Throughout this experiment a variety of factors had the potential to put this study at risk. By risk, it is meant that these following factors would make it so that the samples could not be effectively analysed, subsequently compromising the study.

Contamination was an issue which was deemed to be most prevalent risk. Contamination came from the quartz wool, used to confine the sample within the stainless steel reactor tube. The quartz can be viewed in figure 4.1 where a comparison is present between two samples. It can be seen that the quantity of quartz wool varies, as such is a factor which is difficult to quantify. Initially, to reduce the amount quartz wool residue in the sample, the sample was sieved with a mesh of 400nm. However, the sieving of the sample altered and jeopardised the physical properties of the samples, a factor which is evident to alter the optical spectra. Hence, it was deemed that this was an unnecessary solution to remove the quartz wool. It was also thought to change the confinement material to a glass fibre wool. This too was deemed not to be a valid solution, as the confinement material would be exposed to extremely high temperatures where glass fibre wool would react with the sample. Taking this into account the tests continued to use quartz wool as the confinement material. Fortunately, when analysing the analysis through the FESEM, the quartz wool did not pose a damaging effect on the sample. With this confirmation, quartz wool remained as the confinement material for the sample. Although, to minimise contamination applying and removing the quartz wool was done so with extreme caution.

Furthermore, another factor which threatened to contaminate the samples was the oxidisation of the stainless steel reactor tube. Due to the repeated exposure to high temperatures, cooling and subsequent washing, it was viewed that the stainless steel reactor tube was oxidising. This was proven evident during the SEM characterisation of the samples, which can be seen in figures 4.2a and 4.2b. To remove this risk entirely a quartz reactor tube was proposed, however no reactor tube was present with identical internal diameter to that of the stainless steel reactor tube. This was a factor which could not be ignored as the change in internal diameter would alter the flow speed interacting with the samples. Therefore, the stainless steel reactor tube remained as the tool to house the sample during the hydrogen reduction process. Viewed through the SEM imagery and chemical compositions of the samples, contamination from the stainless steel reactor tube was negligible, verifying the decision to remain with the stainless steel reactor tube.

Figure 4.1: Comparison of two processed samples being exposed to quartz wool

(a) FJS-3/800/120 *(b) FJS-3/800/240*

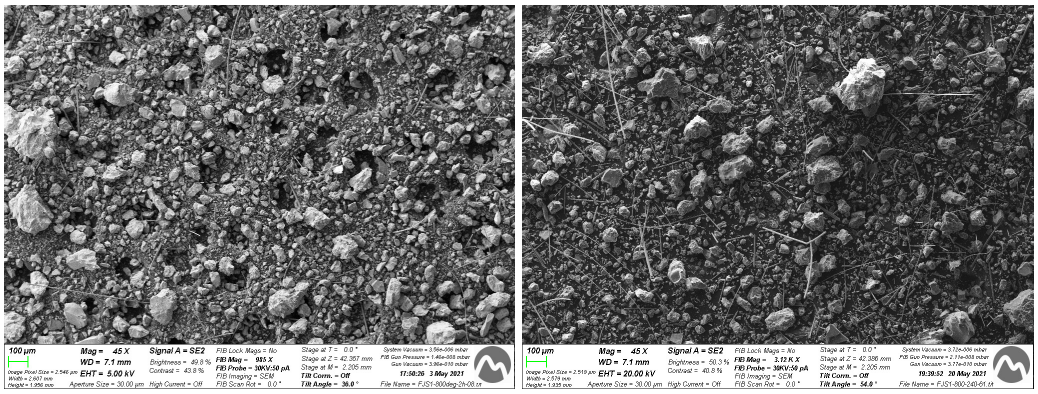

Figure 4.2: 4.2a: Stainless steel displayed within sample JSC-1/800/120. 4.2b: The corresponding elemental composition found in figure 4.2a.

(a)

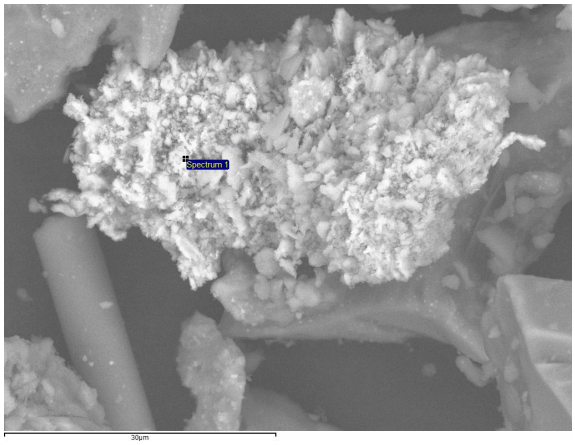

(b)

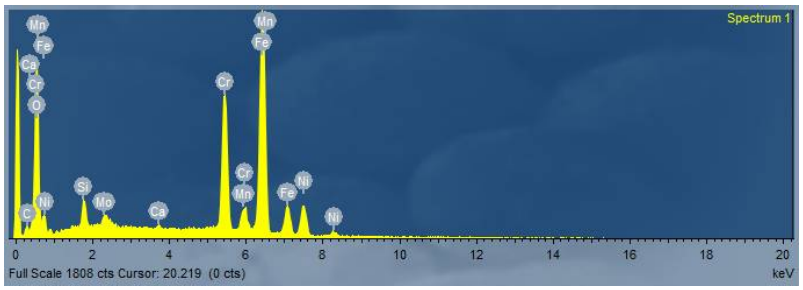

Chapter 5

Results and Discussion

This chapter will display the experimental findings obtained from the procedures that was previously defined. As previously stated , this study sees that the lunar simulants are exposed to a range of temperatures. The time of exposure to these temperatures are 2 hours and 4 hours. Initially the simulants were subjected to 600°C, 800°C and 1000°C for 2 hours. Once all samples have been processed at the desired temperatures, the simulants are then exposed, at the same temperatures, for 4 hours. Based off of previous experiments increasing the time exposing the simulants to the hydrogen flow at high temperature increases the conversion of the sample [8, 11], hence why the duration will be increased. Information gathered from the same papers specifies that, although increasing the temperature increases the reduction of the iron oxide, it also promotes sintering and clumping, a factor in which stunts the reduction process and may develop by increasing reduction duration. Nevertheless, with the maximum temperature of the Carbolite furnace being 1200°C these temperature will remain constant whilst only changing the duration of the test. To finalise this phase of testing, the samples are then catalogued and analysed through an FESEM, gaining a preliminary view of the reaction which has taken place. Through this locating metallic iron, key for the experiment to continue onto the next phase of testing, will be achieved.

Once the categorisation of the sample is complete, optical properties of the samples are tested in the UV-VIS range. The spectra produced will be analysed in order to determine any correlation between the changing optical characteristics and the reduction of the lunar samples. In addition to this, a processed sample will be selected for the Mössbauer analysis. Selection will be based off of the FESEM preliminary characterisation (this will be further explained later in this chapter).

It must be stated that all samples were weighed at 0.50g $\pm$ 0.005g. All reduction processes took place at atmospheric pressure (1bar) and exposed to a flow of 50ml/min. With both the volume flow speed, $\dot{V}$, and the internal diameter of the reactor tube, d, defined, the flow speed, v, can be computed, as seen below.

$$\begin{aligned} \dot{V} &= 50ml/min \\ &= 0.833333ml/s \\ &= 833.333mm^3/s \end{aligned} \tag{5.1}$$

$$\begin{aligned} A &= \frac{\pi * d^2}{4} \\ &= 50.27mm^2 \end{aligned} \tag{5.2}$$

$$
\begin{aligned}
v &= \frac{\dot{V}}{A} \\
&= \frac{833.333}{50.27} \\
&= 66.31mm/s \\
&= 6.63cm/s
\end{aligned} \tag{5.3}
$$

Evident from equation 5.1, the flow speed of the hydrogen is 6.63cm/s. Comparing this to the flow rate provided in [8], where it states that 1cm/s mitigates sintering and clumping. A reasonable assumption can be made that the temperatures implemented in this study will not cause sintering nor clumping within sample.

5.1 Preliminary SEM characterisation of the lunar simulants

Previously mentioned both secondary electrons and backscattered electrons are utilised in order to view the topography of the samples, and to locate metallic iron. Initially the unprocessed samples are viewed, which is displayed in figure 5.1. Consistent with the findings in [51], the elongation of the FJS simulant is smaller when compared to that of the JSC-1 simulant. Additionally, it can be viewed that the FJS-3 simulant is much finer than that of the JSC-1. It can therefore be expected that FJS-3 may produce more metallic iron due to the finer grains - a correlation that is seen within [10]. The scale of the perspective seen in both figures 5.1a and 5.1b is at 100μm, providing a consistent source for comparison. The images displayed in figure 5.1 were produced via the emitted secondary electrons and detected by the corresponding detector.

Figure 5.1: Unprocessed lunar simulants.

(a) JSC-1

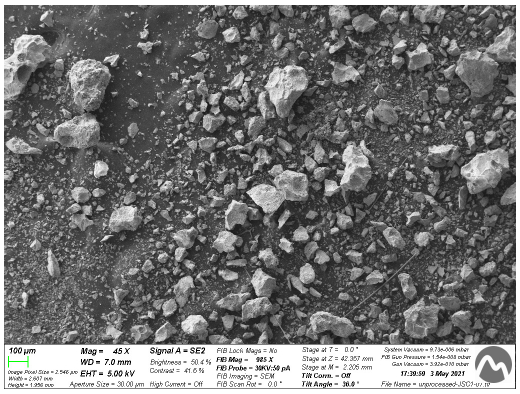

(b) FJS-3

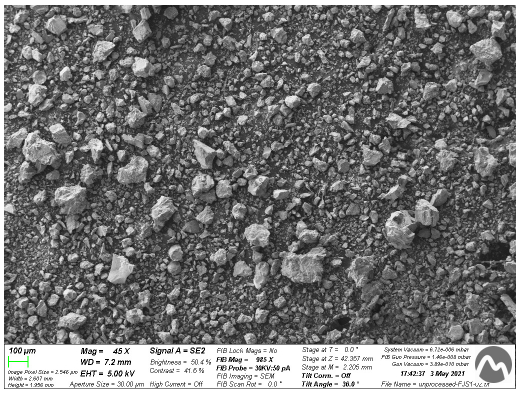

5.1.1 Characterisation of the Processed Lunar Simulants

The test conditions for the hydrogen reduction have been previously defined, but to simplify referring to a specific sample i.e. calling out the tested lunar simulant, the temperature at which it was reduced, and the duration of the reduction, the following code shall be used: lunar simulant/temperature of reduction/duration of reduction. For example, when referring to FJS-3 being reduced at a temperature 800°C for 4 hours the referring code will look like FJS-3/600/240 - the duration of reduction is referred to as minutes.

The aim of this characterisation is to determine whether the iron oxide present. The images displaying the elemental composition of the samples were obtained through the INCA software [59] which uses data acquired from the EDS detector within the FESEM and generates a spectrum representing the elemental composition of the site in question. In addition to this, utilising the scales which are present in the backscattered and secondary electron detected images, the size of the metallic iron particles can be estimated. All samples were viewed through backscattered and secondary electrons, if a view within the tested sample was deemed as a ”site of interest” the elemental composition of said site was collected.

Figure 5.2: 5.2a: JSC-1/600/120 site of interest. 5.2b: The corresponding composition recorded from the spectrum 1 location seen in 5.2a.

(a)

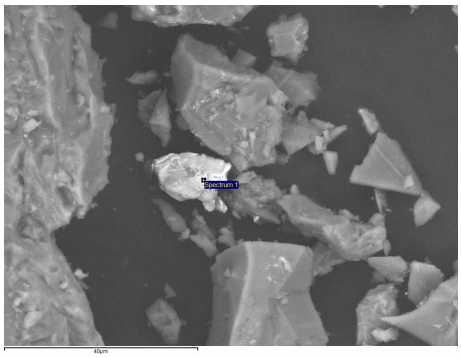

(b)

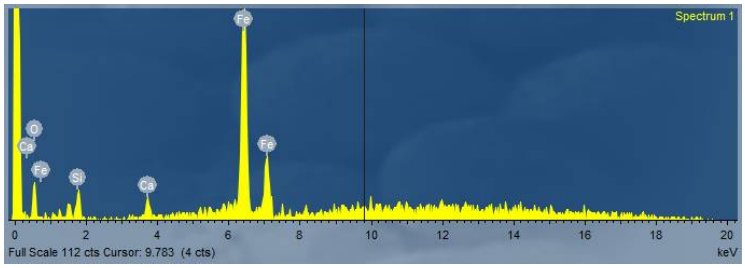

The JSC-1/600/120 sample presented multiple sites of interest, therefore the compositions of these locations were all recorded. Figure 5.2a displays first site of interest. It can be seen that the brightness of the grain in question is far greater than that of its surroundings. Potentially providing initial evidence of the presence of SMFe. Figure 5.2b shows the corresponding composition of the sample, specifically analysing the location labelled spectrum 1 in figure 5.2a and generating evidence that iron has in fact reduced to its metallic form. In order to gain a better estimation of both the scale of the newly formed metallic iron, and the composition within this particle the magnification of the microscope is increased. Figure 5.2a demonstrates a scale of 40μm, by increasing the microscopes magnification the scale now seen in figure 5.3a is 10μm. Through this magnification it is clear to see that the grain present in both figures has a major axis of above $10/mu$m. A more specific estimation indicates the major axis of the particle is roughly 12μm.

A noticeable effect that has appeared in figure 5.3b is the increase presence of oxygen, when comparing it to the composition which is displayed in figure 5.2b. With the increase in oxygen it appears that the metallic iron is forming on the surface of the grain,

Figure 5.3: 5.3a: Magnified view of the grain seen figure 5.2a. 5.3b: The composition data gathered from the perspective seen in figure 5.3a.

(a)

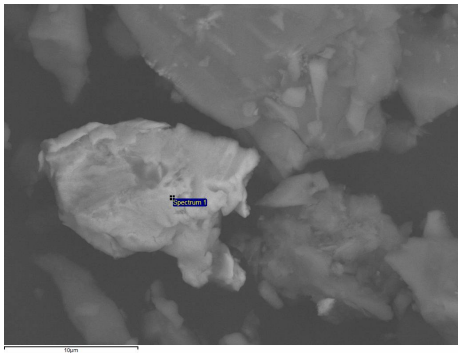

(b)

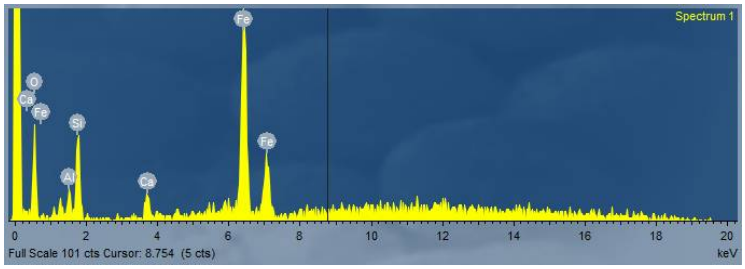

a sight which is coherent with that seen from the products of space weathering. On top of this, by viewing the other elements present in the elemental composition analysis (referring to figure 5.3b) the metallic iron has formed on a host grain of a silicate mineral. Suggesting that the metallic iron has formed without the aid of any metallic oxide compounds. With this being said it was decided to increase the magnification in order to gain a better view of the SMFe forming on the surface of this silicate grain.

Figure 5.4: 5.4a: Further Magnified view of the grain seen in figure 5.3a. 5.4b: The corresponding composition measured from the location seen in figure 5.4a.

(a)

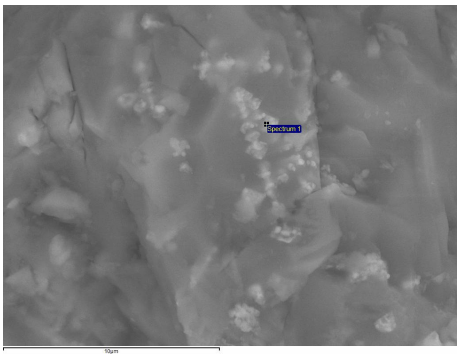

(b)

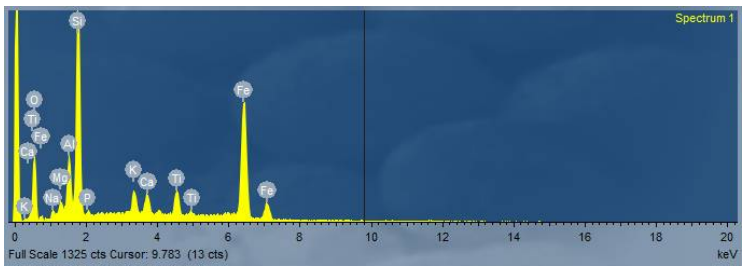

Figure 5.4a provides further evidence to the formation of SMFe has occurred on the surface of this silicate. It can be seen that multiple blebs have in fact formed, clearly being far less than the scale of 10μm, provided in figure 5.4a. Seen in figure 5.4b the presence of silicon has significantly increased, especially when compared to the measured presence of silicon in figure 5.2b. This can be explained by the fact that the perspective, seen in figure 5.2a, clumps the SMFe iron. Essentially masking the host grain causing the elemental composition data displayed in figure 5.2b to indicate that there is a significant amount of metallic iron and very little silicon or oxygen present within the grain. Nevertheless, the figures 5.2, 5.3 and 5.4 clearly demonstrate that reduction has indeed been induced within the sample JSC-1/600/120. Proving that reduction can occur at a reduction temperature of 600°C with a duration of 2 hours.

The next location tested for its composition was within the sample FJS-3/800/120. The first site of interest was tested in two locations, allowing the ability to understand what elements are present with reference to the brightness emitted by the backscattered electrons. The initial scale seen in figure 5.5 is 20μm. Figure 5.5 displays a clear perspective of the different particles within the sample. Visible in figure 5.5a is the particle in question, as it is significantly brighter than that of the surrounding particles. Whereas, the particle selected in figure 5.5b has an equivalent brightness when compared to its surroundings.

Figure 5.5: First site of interest within the sample FJS-3/800/120.

(a) First location where the elemental composition was acquired.

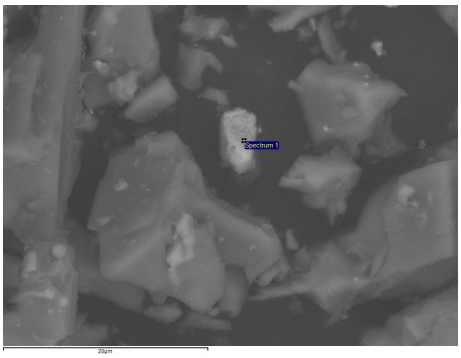

(b) Second location where the elemental composition was acquired.

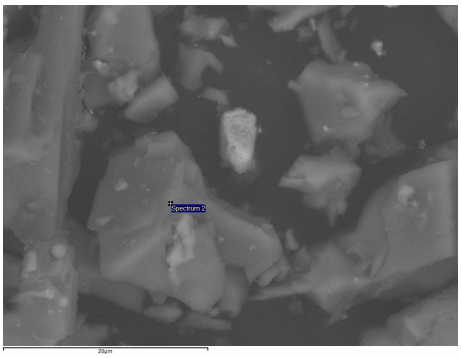

Evident through figure 5.6a, the areas in which appear brighter, when viewing the backscattered electrons, represents an area of reduction. A observation which is consistent with the conclusion formed from analysing the JSC-1/600/120 sample. Backing up this suggestion the elemental composition, seen in figure 5.6b, the dimmer location represents an area where very little reduction has occurred. In regards to the elemental

composition seen in figure 5.6a, and the perspective in which this data was gathered from - the view seen in figure 5.5a. The information gathered from the JSC-1/600/120 analysis must be taken into account - at relatively low magnifications, the metallic iron formed on the surface of the host grain masks the host grain's compositions signal. It can also be seen that the size of the SMFe particle are significantly smaller when increasing the microscopes magnification (referring to both figures 5.2a and 5.4a. Therefore, only conclusion which can be formed from this magnification is that the brighter areas display locations of reduction and dimmer areas display areas if little to no reduction.

Figure 5.6: Elemental composition gained from first site of interest within FJS-3/800/120.

(a) Elemental composition corresponding to the location selected in figure 5.5a.

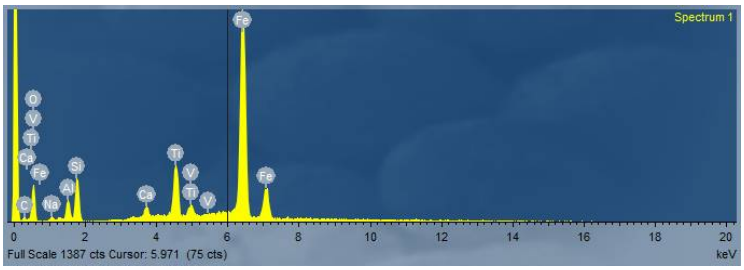

(b) Elemental composition corresponding to the location selected in figure 5.5b.

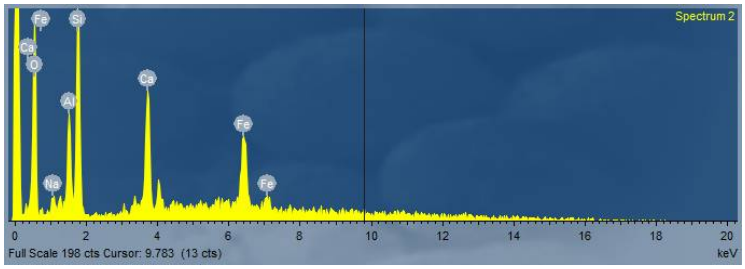

Figure 5.7: 5.7a: The second site of interest selected within the sample FJS-3/800/120. 5.7b: The corresponding elemental composition of the location tested in figure 5.7a.

(a)

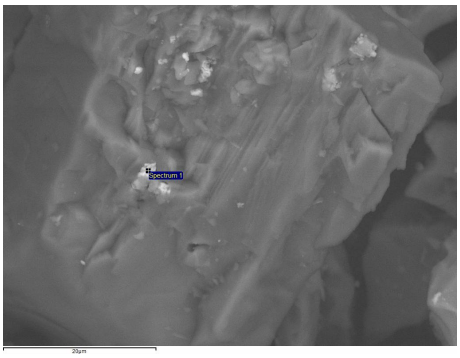

(b)

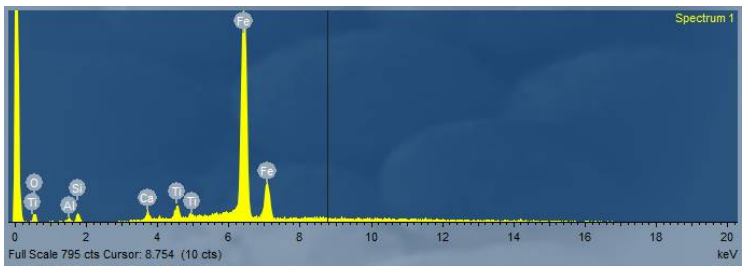

In order to back up the previous statement made - the areas in which appear brighter corresponds to area where reduction, a second site of interest is selected. Figure 5.7b demonstrates this second site and displays a bright bleb. Figure 5.7b confirms that this bright bleb is in fact metallic iron. The scale seen in figure 5.7a is still 20$/mu$m. Utilising this information, the SMFe particles is viewed to be significantly larger than that of the SMFe particles seen in figure 5.4a, given that the scale between these two figures are different, with figure 5.7a's scale being double than that seen in figure 5.4a (unit scale bar of 10μm). Taking this into account, an increased magnification would provide a more definitive conclusion to the SMFe's particle size. However, through this perspective (figure 5.7a) it is clear that this bleb is significantly brighter than that seen in figure 5.3a. Suggesting that an increase in reduction has occurred in the FJS-3/800/120 sample. This can be attributed to two facts: 1) the increase in temperature has generated more reduction, and/or 2) the finer particle sizes in the FJS-3 simulant has caused an increase in reduction. Both of these factors are known contributors to the reduction of iron via hydrogen [11].

The final site of interest within the sample FSJ-3/800/120 can be seen in figure 5.8a. Accompanied by figure 5.8b, it is evident that the site analysed in figure 5.8a is a piece of ilmenite which has clearly not been reduced. Suggesting that the formation of SMFe particles on the surface of silicate host grains appears before the reduction of ilmenite occurs.

Figure 5.8: 5.8a: The third site of interest selected in sample FJS-3/800/120. 5.8b: The corresponding elemental composition seen in the location tested in figure 5.8a.

(a)

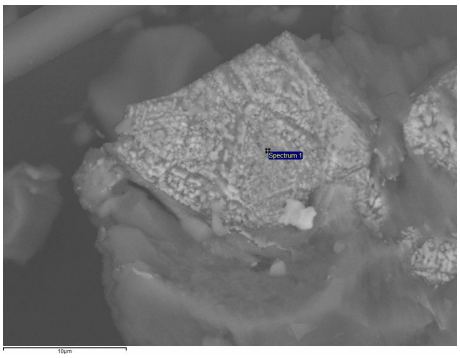

(b)

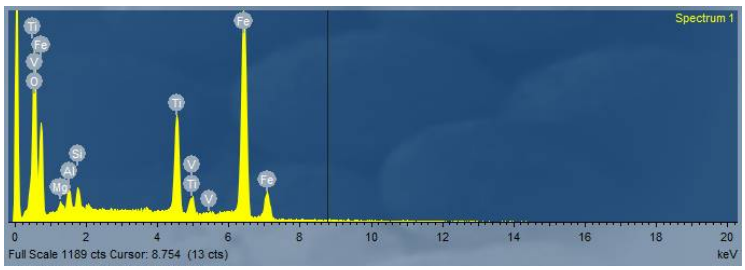

Concluding the samples reduced for 2 hours is the sample FJS-3/1000/120. Noticeably, the brightness differential is substantially greater in figure 5.9a compared to that seen in the previously discussed samples. A difference which appears due to the samples discussed above not being coated in a conductive material. Coating a conductive material to the samples improves the quality of the image produced by the backscattered, improving the brightness differential, allowing for easier determination of site of interests. Proving this, figure 5.9a demonstrates a brightness differential far greater to that seen in figure 5.8a.

Figure 5.9: 5.9a: The first site of interest selected within the sample FJS-3/1000/120. 5.9b: The elemental composition corresponding to the location tested in figure 5.9a.

(a)

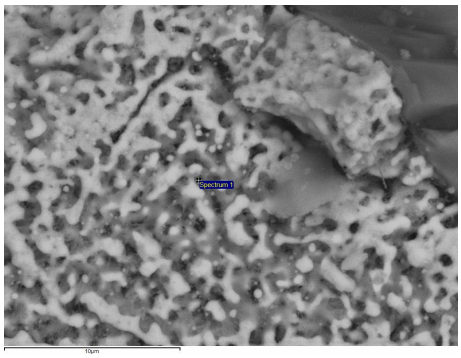

(b)

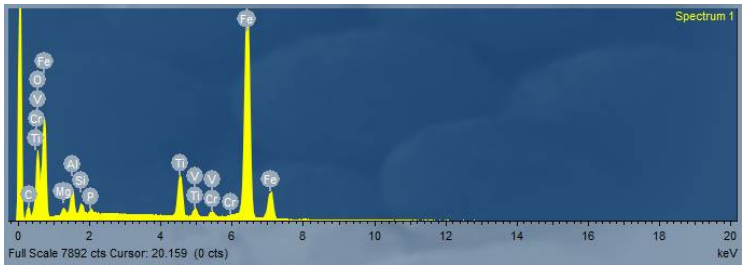

The mineral seen in figure 5.9a shows an appearance which is consistent with that of the ilmenite seen in figure 5.8a. Backed up by the traces of titanium seen in figure 5.9b, this mineral that is being analysed is confirmed to be ilmenite. However, viewing the elemental composition of this ilmenite particle, it can be seen that it has reduced, with a prominent presence of iron within the mineral. To gain a better view of this, a linescan is implemented. The linescan allows a spectrum of the elemental composition to form, providing key information of the particles composition across multiple areas of the tested

particle. The position of the linescan can be seen in figure 5.10.

Figure 5.10: A magnification of the particle seen in figure 5.9a and showing the position of the linescan implemented.

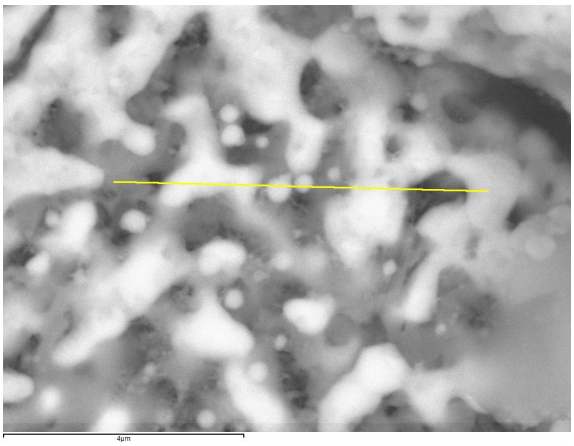

The scale seen in figure 5.10 displays a unit bar of 4μm. Demonstrating a significant increase in magnification from the perspective seen in figure 5.9a (a unit bar of length 10μm). The line spectra displayed in figure 5.11a provides evidence that the areas which are brightest constitute to areas were metallic iron has formed (blue = iron, oxygen = yellow and titanium = green). With the scale being seen as 4μm it is clear that size of the metallic iron formed is far greater than that seen in any of the previous samples. Clearly the reduction of ilmentite is partially dependent on the temperature of reduction, seeing that in the sample FJS-3/800/120 the ilmenite analysed had not yet been reduced.

Figure 5.11: 5.11a displays the elemental composition spectrum. 5.11b: displays the same spectra seen in figure 5.11a, along with the definition of each spectrum.

(a) *(b)*

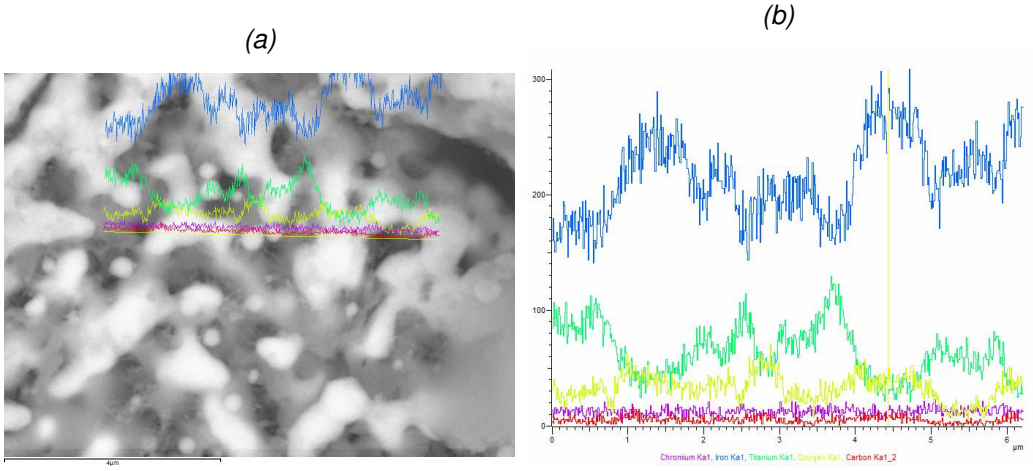

This concludes the characterisation of the sample that were reduced for 2 hours and marks the beginning of the analysis of the sample which were tested for 4 hours. It must be said that only the samples which displayed a behaviour that is deemed essential to discuss will be presented with an in depth analysis. This is due to the fact that most samples demonstrated the same behaviour of that seen in the samples discussed above.

Nevertheless, samples such as: FJS-3/600/240 and JSC-1/600/240 displayed consistent characteristics to that seen in their 2 hour reduced counterparts. Figure 5.5 demon-

strates how a larger amount of iron blebs are forming on the surface of a silicate particle, when compared to the particle analysed in both JSC-1/600/120 and FJS/800/120. The term ”forming” is used to describe what is seen in figure 5.12a as the elemental composition demonstrated in figure 5.12b displays strong signals oxygen and the silicate mineral. Evidently, the reduction of iron has not been fully completed within the FJS-3/600/240 sample.

Figure 5.12: 5.12a: Site of interest within the sample FJS-3/600/240. 5.12b: The corresponding elemental composition of the selected tested location within figure 5.12a.

(a)

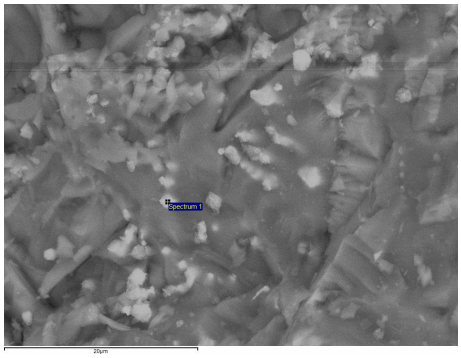

(b)

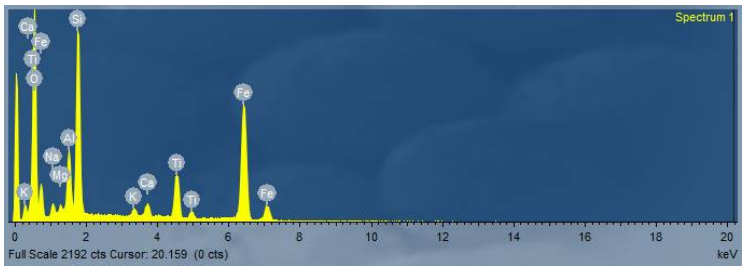

A notable occurrence which is seen in the JSC-1/1000/240 sample is the reduction of the silicate mineral. The site of interest being analysed in this aspect is shown in figure 5.13. The analysis implemented allows to map this entire area’s elemental composition, which can be seen in figure 5.14. Through this analysis it can be confirmed that the statement made when referring to figure 5.4, that SMFe is forming on a silicate material without the aid of a metallic oxide present. This only needs to be proven by viewing figure 5.14 where there is a substantial amount of metallic iron present where there is a severe lack of silicon and oxygen (referring to figures 5.14c, 5.14d and 5.14f).

This concludes the characterisation of the lunar simulants tested in this phase. It can be summarised that the reduction of iron has taken place throughout all the tested samples. Providing key information that will be utilised when inspecting the optical spectra formed from these tested samples.

Figure 5.13: Site of interest within JSC-1/1000/240.

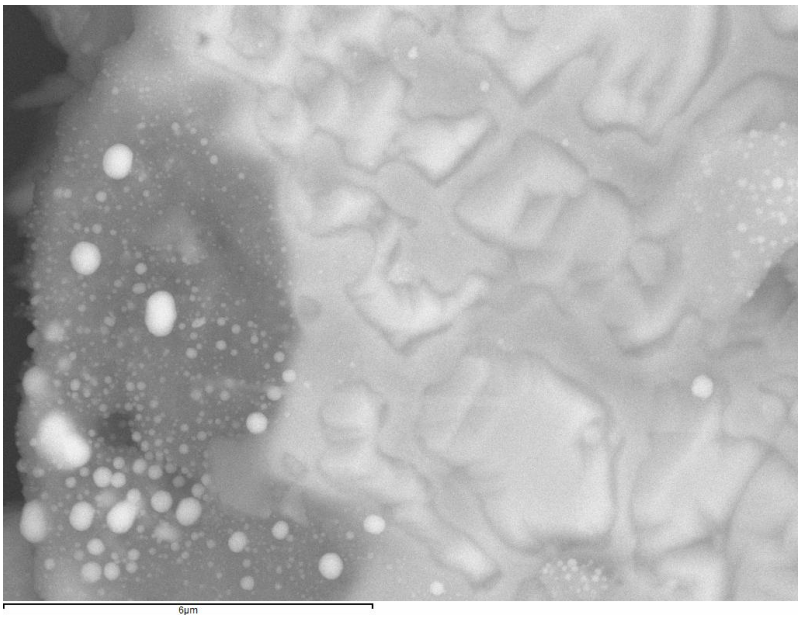

Figure 5.14: Elemental composition map corresponding to the site seen in figure 5.13.

(a) Aluminium

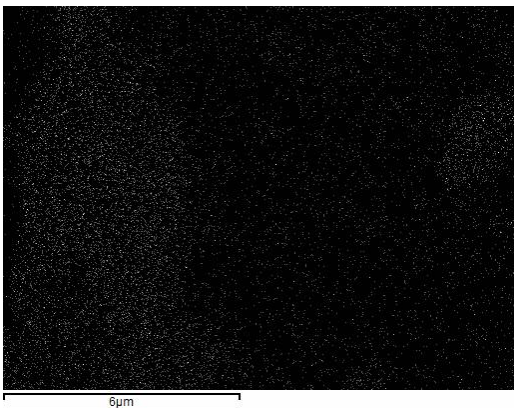

(b) Carbon

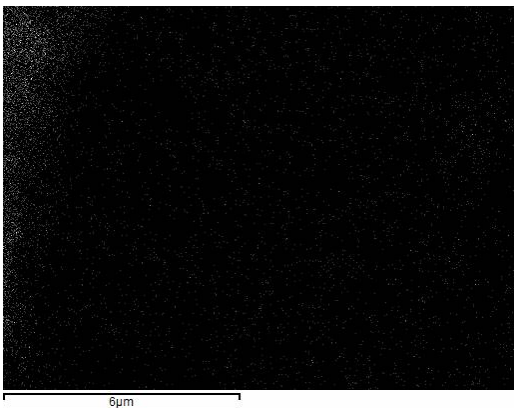

(c) Iron

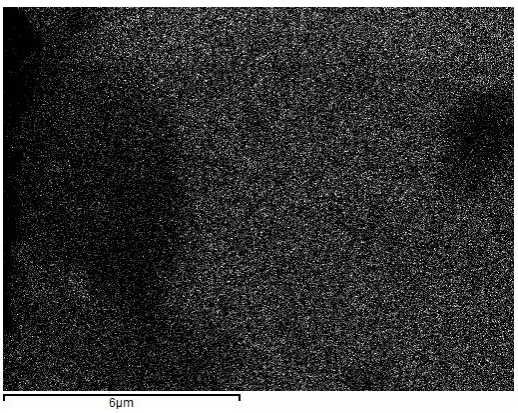

(d) Oxygen

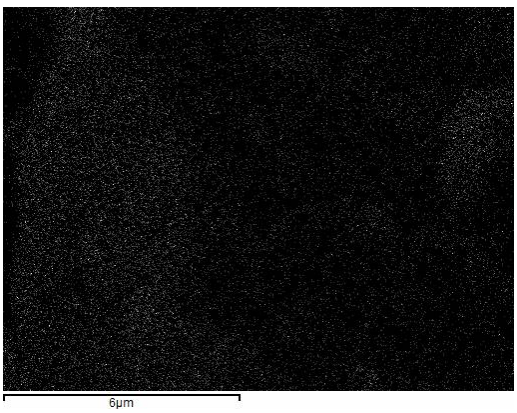

(e) Phosphorus *(f) Silicon*

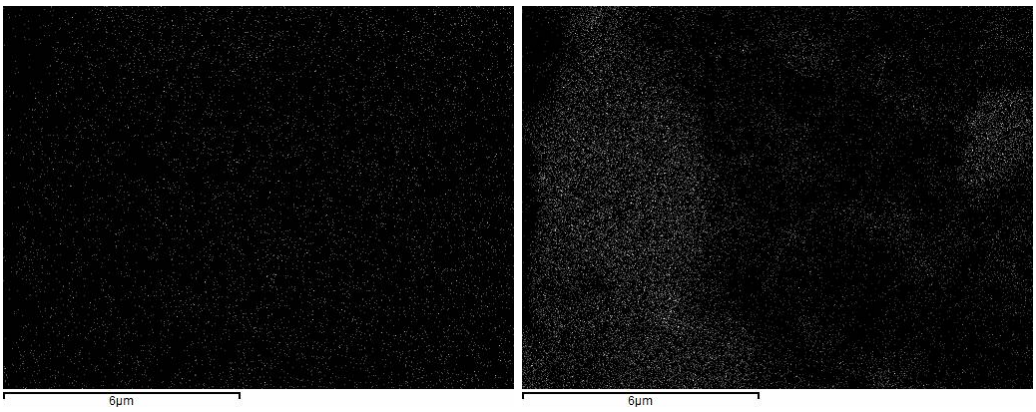

5.2 UV-VIS Spectroscopy

To initialise this analysis, calibration is required. Calibration is needed to determine the wavelengths in which significant noise occurs. Noise is necessary to locate as it will impact the analysis of the sample's optical properties. The spectra produced from this calibration is known as the baseline. These baseline spectra can be seen in figure 5.15. Batches refers to the sample which were tested in a single session, as the testing of the samples spanned over three sessions, three baselines are displayed in figure 5.15. Samples that were tested in these batches goes as follows: 1^{st} batch) JSC-1 and FJS-3 at 1000°C for 4 hours; 2^{nd} batch) both JSC-1 and FJS-3 at 600°C, 800°C and 1000° for 2 hours, then at 600°C and 800°C for 4 hours. It was found that one of the samples fell into to the testing chamber, compromising the samples JSC-1 at 800°C for 4 hours and FJS-3 at both 600 and 800°C for 4 hours. Therefore, these samples were tested once again in the 3^{rd} batch of testing.

Figure 5.15: Baseline spectra on each batch.

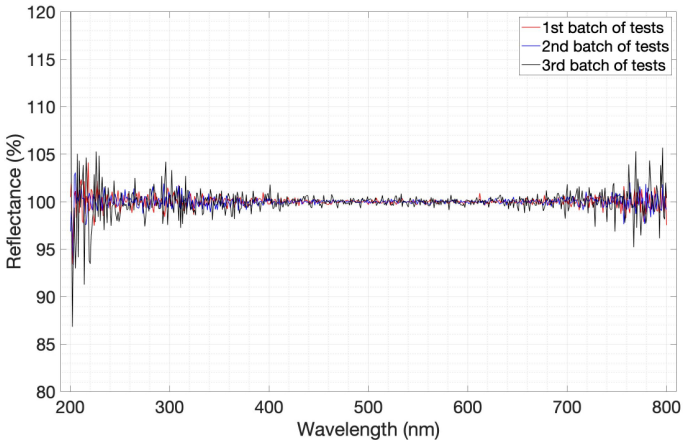

Figure 5.15 demonstrates a clear area where the PMT detector is most reliable, in the range of 400nm to 700nm. However, the PMT detector produces a great amount of noise at either end of its detecting range. This noise is generated due to the wavelengths being at the limits of the PMT detector (refer to table 4.1). A factor which must be taken into account in the later analysis of the sample's optical properties. It must be noted that the noise generated from the third batch is significantly larger than that generated in the first

and second batches. This is evident in figure 5.16 where the noise is significantly less when compared to the noise seen in figure 5.15. Therefore, a comparison is conducted between the 2^{nd} batch and 3^{rd} batch, to deem whether the samples tested in the 3^{rd} batch can be rejected. This is a factor analysed to determine whether the spectra produced in the 2^{nd} batch follows the same characteristics seen from the 3^{rd} batch. If a correlation can be seen, then the contamination which incurred during the 2^{nd} batch can be deemed as being negligible.

Figure 5.16: Baseline spectra of the 1^{st} and 2^{nd} batch.

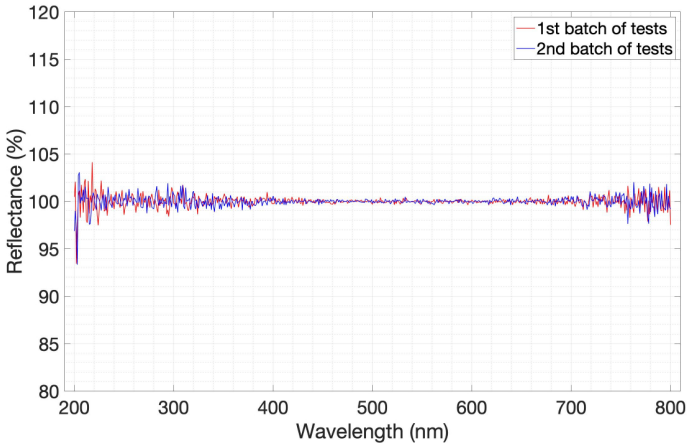

Figure 5.17: A comparison between the spectra collected in the 2^{nd} and 3^{rd} batches.

(a) JSC-1 at 800° C for 4 hours.

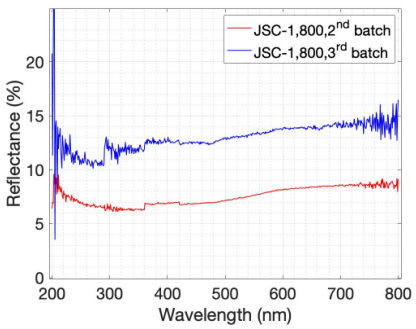

(b) FJS-3 at 600° C for 4 hours.

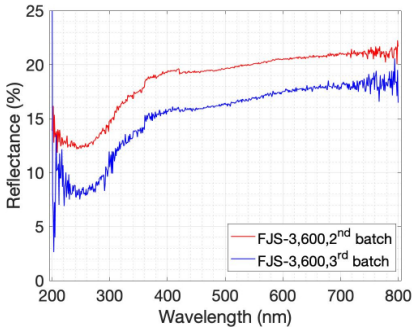

(c) FJS-3 at 800° C for 4 hours.

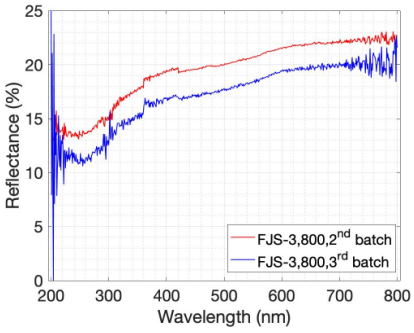

Throughout the images seen in figure 5.17 the spectra produced from both the 2^{nd}

and 3^{rd} batch is compared. Evidently ,the same general curve can be seen for all samples tested. However a difference can be seen in the reflectance of the compared samples. This difference is seen to be less significant when viewing the error which is produced within the 3^{rd} batch of tests. Taking this into account, for the remainder of this analysis the spectra produced in the 2^{nd} batch of tests will be continued to be analysed, disregarding the spectra produced in the 3^{rd} batch.

5.2.1 Optical Properties of Lunar Simulant JSC-1

Figure 5.18: JSC-1: 2 hours of reduction.

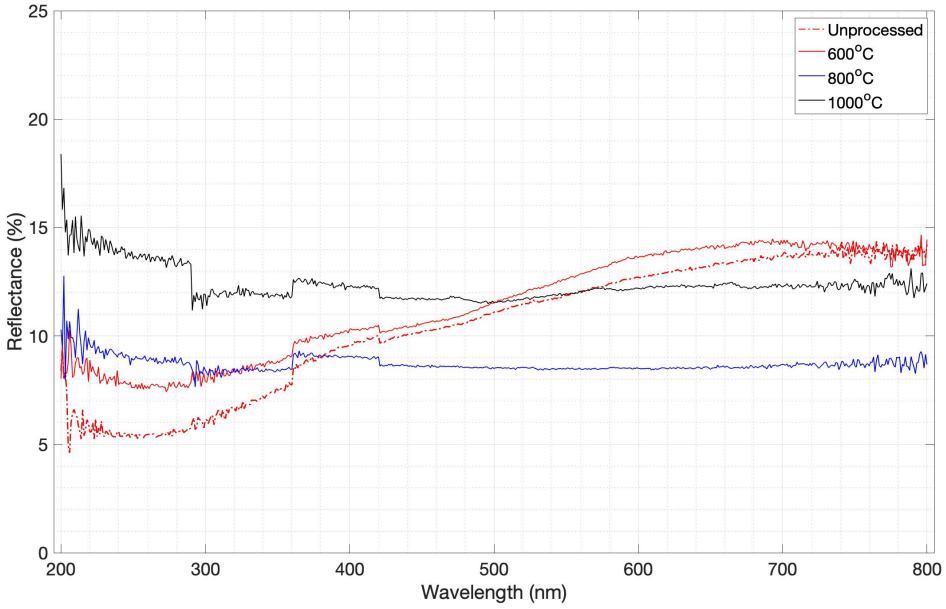

Displayed in figure 5.18 is the optical spectra of the lunar simulant JSC-1, reduced at 600°C, 800°C and 1000°C, it also includes the unprocessed JSC-1 reflectance spectrum. It must be noted that the same code defining the lunar simulant, the reduction temperature, and the duration of reduction shall be used, in order for consistency and the simplification of referencing.

It is evident that by increasing the temperature of reduction, the reddening of the spectra severely reduces. This can be attributed to the production of metallic iron within the sample, an effect that can be seen to occur in studies such as [21]. Conversely, JSC-1/1000/120 is significantly more reflectant than that of the sample JSC-1/800/120. Referring to figure 2.5, an image gained from [21], it is possible that the increase of reflectance correlates with increasing size of metallic iron. Elaborating upon this, as the temperature of reduction increases, it is possible that the size of the metallic iron present in the sample is also increasing. This does not just mean an individual metallic iron particle, as is seen through figures 5.2, 5.3a and 5.4 as the magnification of the microscope increases, the host grain is more apparent in the elemental composition data. Therefore, a plausible reasoning for the increase of relfectance is due to an increasing abundance of SMFe or npFe^0 in a given location within the sample, subsequently assuming the behaviours of a larger SMFe.

In addition to the darkening of the spectra, it can be seen that a peak of absorption develops in the range of 360nm - 420nm, due to the fact that this appears uniformly through most of the spectra - appearing in the same range of wavelengths and develops so suddenly. This is accredited to an instrumental artifact present from the UV-3600. Taking this into account, this peak in the spectra can now be seen as an anomaly, and will be assumed that the spectra would follow the same characteristics both previously and subsequently to the occurrence of the peak if the instrumental artifact was not present.

Figure 5.19: JSC-1: 4 hours of reduction.

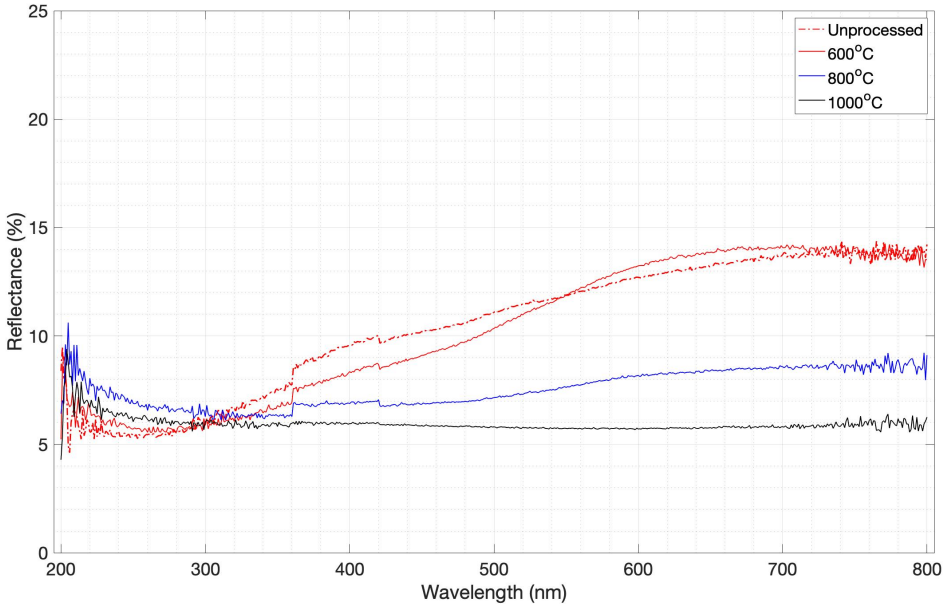

Consistent with that seen in figure 5.18, figure 5.19 demonstrates a clear darkening of the sample's spectra as the reduction temperature increases. This consistency adds evidence to an increasing amount of metallic iron present in the samples. Based off of the optical properties seen in figure 2.5, and the size of metallic iron groupings seen in the SEM characterisations either the individual or effective abundances of metallic iron is in the 100's of nanometers. Contrasting that seen in figure 5.18, sample JSC-1/1000/240, seen in figure 5.19, is slightly less absorbent than that of the 800°C sample. Eluding to the fact that the sudden increase of relectance seen in figure 5.18 is not due to the presence of large metallic iron particles. On the other hand, potentially larger metallic iron particles do in fact appear in JSC-1/1000/120, but due to the fact that JSC-1/100/240 is reduced within an environment for 4 hours, there is a possibility that sintering and clumping may have occurred, subsequently darkening the sample's spectrum.

Both figures 5.18 and 5.19 display how the reduction temperature impacts the optical properties of the lunar simulant JSC-1. Next, the two reduction durations shall be compared. Figure 5.20 presents the difference between reducing the sample for 2 hours and reducing the sample for 4 hours. Both figures 5.20a and 5.20b demonstrate a minimal overall change in reflectance within the visible spectrum, but it is evident there is a reddening effect which becomes more prominent when increasing the reduction time from 2 hours to 4 hours. Again using figure 2.5 as a reference, the increase in reddening seen is consistent with the appearance of npFe^0 (to reiterate npFe0 is defined to be metallic iron particles $<$100nm within this thesis), suggesting that with increasing reduction duration

Figure 5.20: Reduction of Lunar simulant JSC-1.

(a) Reduction at 600° C.

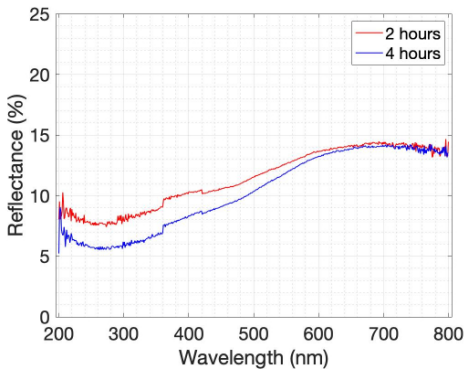

(b) Reduction at 800° C.

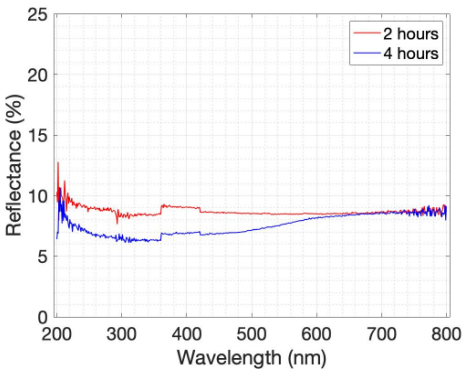

(c) Reduction at 1000° C.

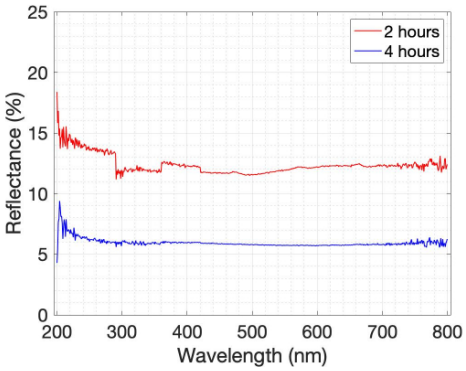

at reduction temperatures of 600°C and 800°C smaller sizes of metallic iron form within the JSC-1 sample.

Taking into account the reduction in reflectance displayed in figure 5.20c, this change coincides with the explanation provided previously. That the sample JSC-1/1000/240 experienced sintering during the reduction process. However, sintering was not viewed within the SEM characterisation. Thus, more work is needed to better describe the change of optical properties seen within figure 5.20c.

5.2.2 Optical Properties of Lunar Simulant FJS-3

Just like the lunar simulant JSC-1, FJS-3 shall be analysed in the same manor. Both figures 5.21 and 5.22 represent the change in optical spectra with varying reduction temperatures. Figure 5.21 presents how a reduction of lunar simulant FJS-3 for 2 hours at given reduction temperatures alters its optical properties. Whereas, figure 5.22 demonstrates how the optical properties of FJS-3 change when increasing the reduction temperature, whilst maintaining a constant reduction duration of 4 hours. To finalise this study of the FJS-3 optical spectra, a comparison will be formed on the two reduction durations, this can be seen within figure 5.23.

It can be seen how the overall reflectance of the FJS-3 simulant remains similar within the visible region of the spectrum (referring to figure 5.21. Whilst an increasing

in reflectance is present within the UV region of the spectrum. Suggesting that FJS-3's reflectance in the UV spectrum correlates to the increasing presence of npFe^0. This will clearly need to be explored further. Although, what can be said now is that there is an increase in UV reflection within the figure 2.5 which is consistent with the increasing UV reflectance seen within figure 5.21. Indicating the appearance of increasing size of metallic iron within the FJS-3 sample.

Figure 5.21: FJS-3: 2 hours of reduction.

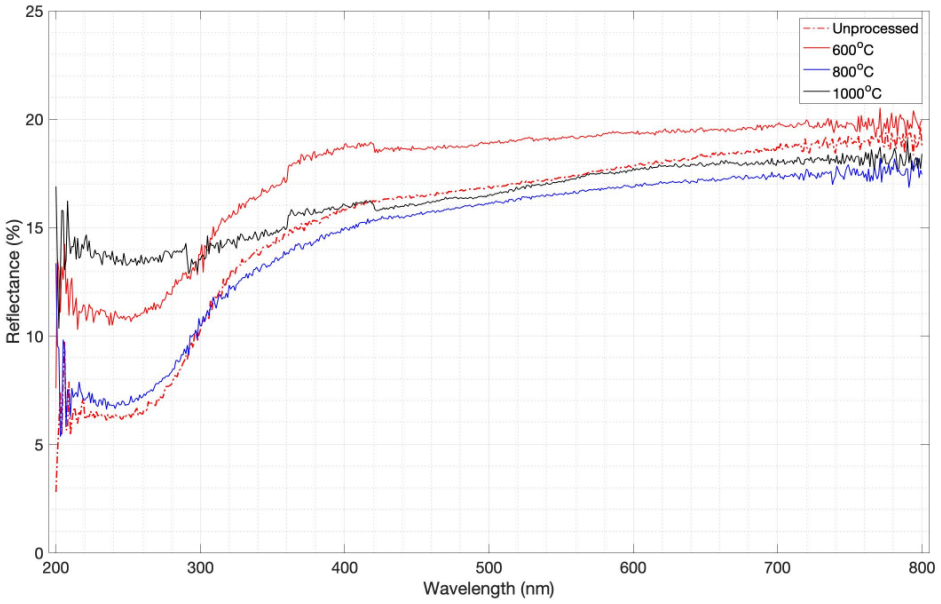

Figure 5.22: FJS-3: 4 hours of reduction.

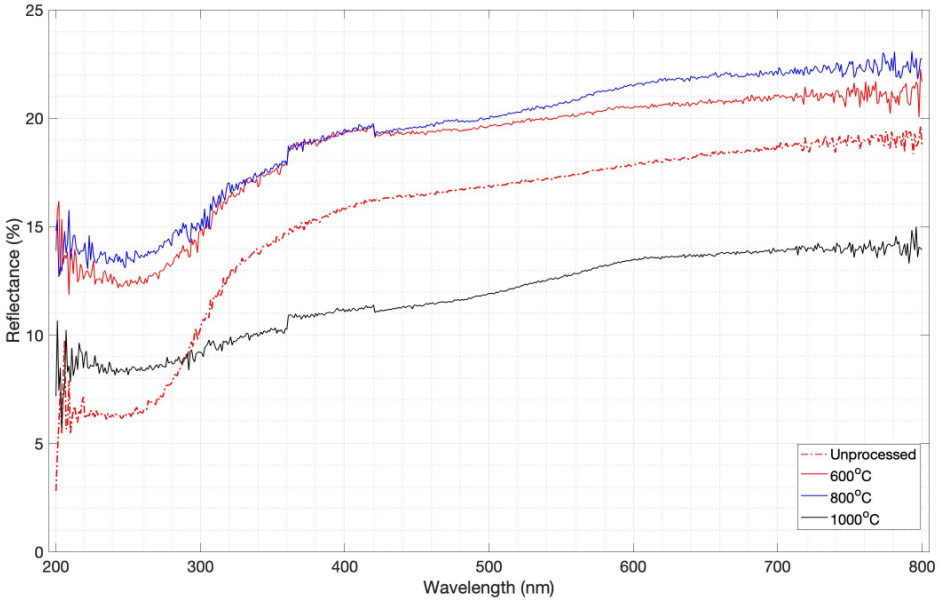

The final characteristic presented in figure 5.21 is the gradual decreasing of redden-

ing seen as the reduction temperature increases. By the FJS-3/1000/120, the optical spectrum is relatively flat compared to the lower reduction temperatures. However, there is still a slight reddening present within the FJS-3/1000/120's optical spectrum, this characteristic will be later elaborated upon.

With regards to figure 5.22, the difference in optical properties present in both FJS-3/800/240 and FJS-3/600/120 samples, and the characteristics produced via FJS-3/1000/240 can be seen that there is an overall reduction in reflectance. A consistent characteristic seen throughout the figures 5.18, 5.19 and 5.21. Another visible characteristic, is the gradual reduction in reddening, where the change in reflectance difference between $\leq$250nm and $\geq$340nm progressively decreases as the reduction temperature increases. Until the spectra produced via the FJS-3/1000/240 sample reaches an almost consistent gradient throughout its spectrum.

Figure 5.23: Reduction of lunar simulant FJS-3.

(a) Reduction at 600° C.

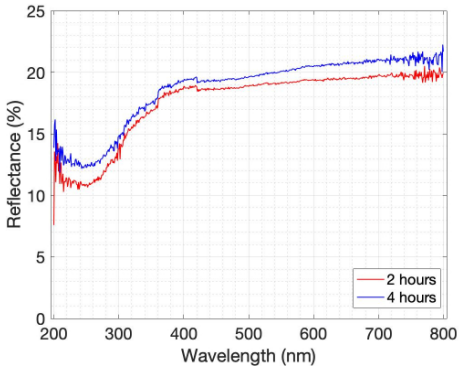

(b) Reduction at 800° C.

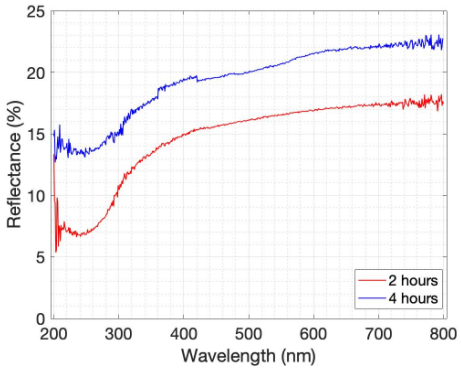

(c) Reduction at 1000° C.

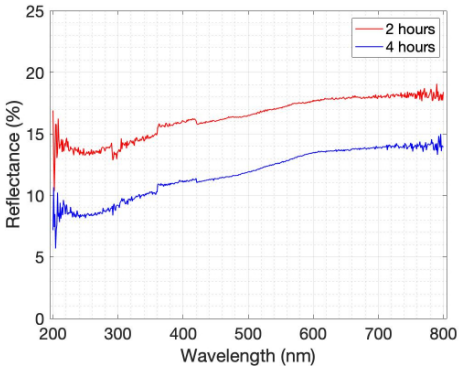

Both figures 5.23a and 5.23b display an increase in reflectance as the reduction time increases. A behaviour which is inconsistent with that seen in figures 5.23c and 5.20. This behaviour can be attributed to the contamination of the sample. With regards to the FJS-3/800/240 sample containing greater amounts of quartz wool when compared to its 2 hour sample (refer to figure 4.1). It must be stated that no evidence has been found confirming that quartz wool impacts the optical spectra in this way, therefore this is just speculation. On the other hand, a potentially more definitive reason for this increase in refectance could be accredited to larger abundances of metallic iron forming within the FJS-3 sample. To demonstrate this, figure 5.24 presents a comparison between

backscattered electron images of FJS-3/800/120 and FJS-3/800/240. The magnification of these two images are relatively similar, both displaying unit bars of 10μm. Therefore the images can be effectively compared. One of these differences that is extremely prominent, is the far greater amount of bright spots within figure 5.24b. Previously discussed, within the SEM characterisation section, these bright spots correspond to locations of reduction, maybe not completely reduced but areas where reduction has occurred. With this being said, it can be seen that the FJS-3/800/240 sample (seen in figure 5.24b) contains a larger quantity of reduced locations. On top of this, these locations are extremely bigger than that seen in the FJS-3/600/120 sample (referring to figure 5.24a). This provides strong evidence for why an increase in reflectance is seen between the FJS-3/800/120 and FJS-3/800/240 optical spectra (displayed in figure 5.23b).

Figure 5.24: Backscattered electron images of the FJS-3 sample.

(a) FJS-3/800/120 *(b) FJS-3/800/240*

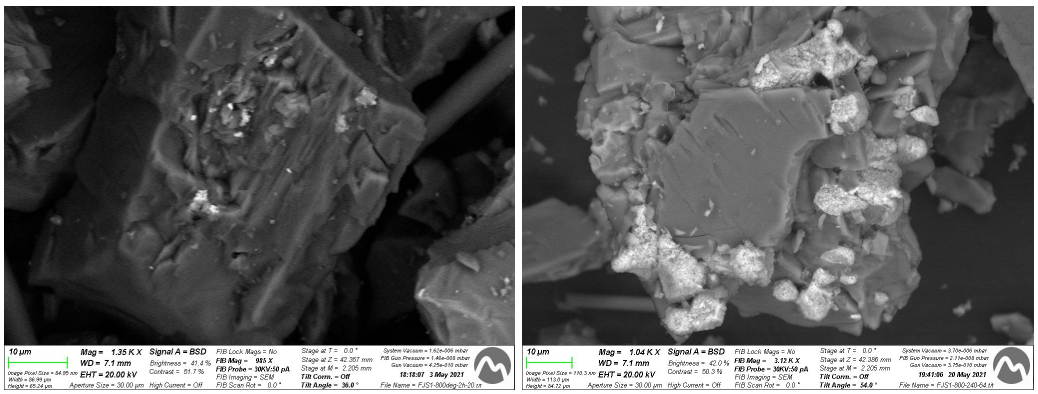

A significant change between the two samples is the altering continuum which is noticeable in both figures 5.23a, and 5.23b. This change correlates to the reduction of the iron oxides, present in FJS-3, to their metallic phase. It can be seen that the reflectance increase is significantly less in figure 5.23a, when compared to the reflectance increase seen in figure 5.23b. The change in continuum is a reference to the overall difference between the reflectance in the UV and visible region. Therefore, basing off of this statement and the spectra displayed in figure 5.23a, it can be seen that there is indeed an increase in reduction within the FJS/600/240 when compared to FJS/600/120.

In terms of the spectrum seen in figure 5.23c, there is a slight reddening within the spectra. Compared to the spectra seen in 5.20c, where it could be said that the JSC spectra is relatively spectrally neutral. To explain the cause of this difference [61] was viewed to determine the spectral characteristics of some of the other substances within the FJS-3 simulant. It was found that the spectral behaviour of Titanium dioxide (TiO_2) shows a great amount of reflectance above 400nm (a sharp increase to 60% reflectance). This proves to be important as a product from the reduction of ilmenite is TiO_2. As previously mentioned, as FJS-3 reduces, both the metallic iron and TiO_2 content within the sample increases. With FJS-3 containing more than three times of TiO_2 than that of the JSC-1 simulant, the TiO_2 can be held responsible for the positive gradient seen in both samples presented in figure 5.23c.

5.2.3 Preliminary Quantification of the UV Reddening Gradient

To better describe the change in optical properties seen through the UV-VIS spectrosciopy analysis, quantification is needed. This is accomplished to attempt to determine a relationship between increasing reduction temperature and reddening reduction. Therefore, the reddening gradient seen in the optical spectra shall be recorded, taking the largest gradient seen within the recorded spectra of both the unprocessed simulants. This is seen to be within the wavelength range of 250nm - 350nm. Therefore, the gradient will be measured in this range of wavelengths throughout all samples. This gradient will be referred to as the reddening gradient. Tables 5.1 - 5.4 displays these gradient values.

Table 5.1: Reddening of JSC-1 sample (2 hours reduction).

Sample ID	**Reflectance at 250nm (%)**	**Reflectance at 350nm (%)**	**Reddening Gradient (%/nm)**
UJSC-1	5.3714	7.5482	0.021768
JSC-1/600/120	7.6391	8.8435	0.012044
JSC-1/800/120	8.8825	8.4632	-0.004194
JSC-1/1000/120	13.5449	11.9131	-0.016318

Table 5.2: Reddening of JSC-1 sample (4 hours reduction).

Sample ID	**Reflectance at 250nm (%)**	**Reflectance at 350nm (%)**	**Reddening Gradient (%/nm)**
UJSC-1	5.3714	7.5482	0.021768
JSC-1/600/240	5.7050	6.7935	0.010885
JSC-1/800/240	6.8893	6.3135	-0.005758
JSC-1/1000/240	6.0405	5.8233	-0.002172

Table 5.3: Reddening of FJS-3 sample (2 hours reduction).

Sample ID	**Reflectance at 250nm (%)**	**Reflectance at 350nm (%)**	**Reddening Gradient (%/nm)**
UFJS-3	6.3875	14.3261	0.079386
FJS-3/600/120	10.8968	16.9649	0.060681
FJS-3/800/120	6.8249	13.4394	0.066145
FJS-3/1000/120	13.3046	14.661	0.013564

Table 5.4: Reddening of FJS-3 sample (4 hours reduction).

Sample ID	**Reflectance at 250nm (%)**	**Reflectance at 350nm (%)**	**Reddening Gradient (%/nm)**
UFJS-3	6.3875	14.3261	0.079386
FJS-3/600/240	12.2434	17.5433	0.052999
FJS-3/800/240	13.5136	17.6404	0.041268
FJS-3/1000/240	8.1497	10.244	0.020943

It is evident through these tables that reddening reduction is consistent throughout the increasing reduction temperatures. It must be stated however that some characteristics of the changing optical spectra are not represented within these preliminary values. For example, seen in figure 5.20a and 5.20b there is a clear increase in reddening. However, when referring to tables 5.1 and 5.2 the presented reddening gradients decrease from the 2 hour reduction to the 4 hour reduction. This is factor that must be taken into account in later studies, but for the case of this thesis the aim of this preliminary calculation is to provide quantitative value pairing the reducing reddening and the increase in reduction temperatures, which it has succeeded in conveying.

The reddening gradient is plotted and displayed in figure 5.25. Presenting a clearer view of the correlation between the reddening gradient within the UV region and the reduction temperature. In addition to this, figure 5.25 provides an opportunity to compare the reddening reduction between the 2 hour and 4 hour reduction process. The data points located at 0°C corresponds to the unprocessed lunar simulants.

Evidently, the reddening gradient does indeed reduce with increasing reduction temperatures. Noting that in two cases, JSC-1/1000/240 and FJS-3/800/120, the reddening gradient increases from their previous reddening gradient data point. In order to determine whether this is an anomaly or a consistent behaviour pattern seen in this relationship, multiple data points will need to be obtained. Adding to this, to aid in finding a more definitive correlation between the reddening gradient and reduction temperature, more test will need to be ran at an increase number of reduction temperatures. Proposing to initially process the lunar simulant samples at intervals of 50°C starting from 600°C.

Figure 5.25: Plots demonstrating the change in reddening with increasing reduction temperatures.

(a) JSC-1 *(b) FJS-3*

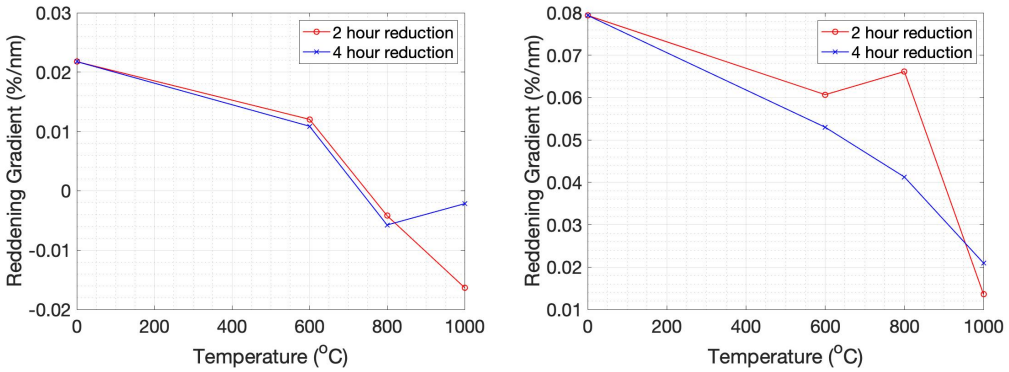

The next step in analysing these reddening gradient plots is fitting an equation to describe the relationship seen in figure 5.25. Due to the occasions where the reddening gradient increases from the previous data point a polynomial curve is deemed to hold the best potential the describe the relationships seen throughout figure 5.25. To obtain this fitted equation, Matlab was utilised by implementing the polyfit tool. Table 5.5 displays the polynomials that were acquired for each plot seen in figure 5.25, where T represents the reduction temperature.

Figure 5.26 displays these polynomial equations defined in table 5.5, and the corre-

sponding experimentally retrieved reddening gradients. The equations generated offer a preliminary method of determining the reddening gradient within the UV region for both lunar simulants, JSC-1 and FJS-3, at a variety of reduction temperatures. As previously mentioned, a relationship is noted to be apparent between the reddening gradient of the optical spectra within the UV region, and the production of metallic iron. Therefore with further development, an equation linking reduction temperature and reddening gradient, and subsequently the content of metallic iron, posses great aid in optimising a hydrogen reduction reactor for the future utilisation of lunar resources via the lunar regolith.

Table 5.5: Polynomial equations defining the relationship seen in figure 5.25.

Sample ID (Lunar simulant/duration of reduction	**Fitted Polynomial Equation**
JSC-1/120	$1.7057 * 10^{-19}T^6 - 1.8055 * 10^{-16}T^5 - 2.8104 * 10^{-14}T^4 + 0.021768$
JSC-1/240	$3.3113 * 10^{-19}T^6 - 3.7973 * 10^{-16}T^5 + 2.4655 * 10^{-14}T^4 + 0.021768$
FJS-3/120	$-1.8187 * 10^{-18}T^6 + 3.1062 * 10^{-15}T^5 - 1.3533 * 10^{-12}T^4 + 0.079386$
FJS-3/240	$-8.9079 * 10^{-11}T^3 + 1.0673 * 10^{-7}T^3 - 7.5729 * 10^{-5}T^2 + 0.079386$

Figure 5.26: Comparison between the reddening gradient computed from the lunar simulants optical spectra and the polynomial curve fitted to said reddening gradient data.

(a) JSC-1/120

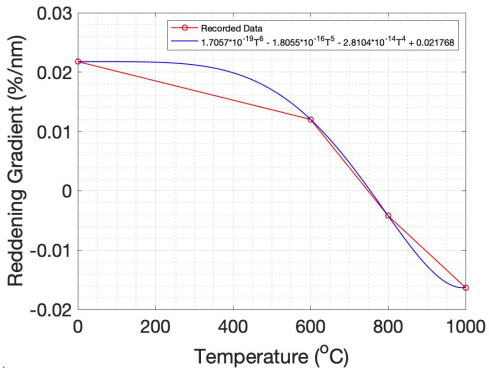

(b) JSC-1/240

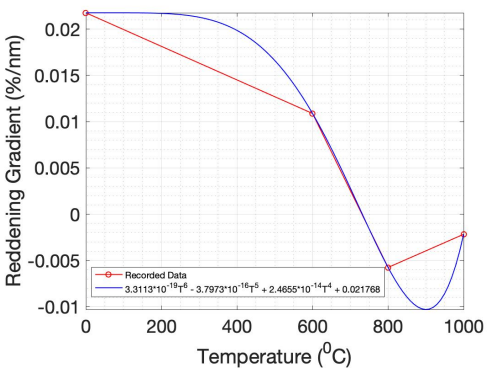

(c) FJS-3/120

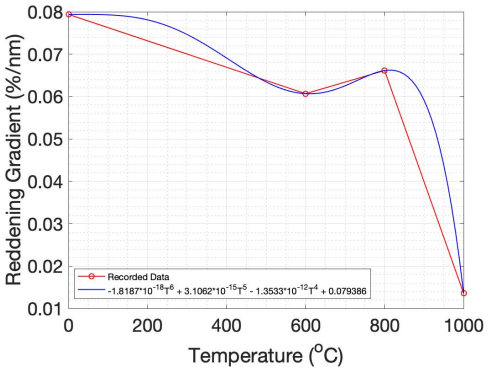

(d) FJS-3/240

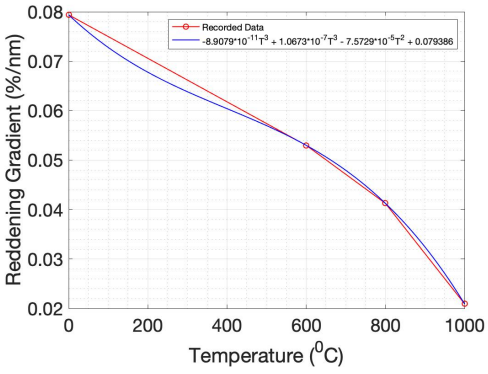

Through figure 5.26 it is clear that more data is needed in order to form a more definitive consensus on the correlation between the UV reddening gradient and the reduction temperature. With the formation of a certain correlation a more accurate equation can be fitted to the data point, subsequently better describing the relationship and posing the opportunity for far more accurate interpolations to be accomplished. However, with this being said, figure 5.26a, 5.26c and 5.26d display relatively well fitted curves for the minimal data point available, providing a suitable equation for preliminary interpolation.

5.3 Mössbauer Analysis of the JSC-1 Lunar Simulant

A preliminary analysis using Mössbauer equipment was implemented to gain a first view of the exact amount of iron present in the reduced sample. Only two samples were selected for this analysis, one had to be the unprocessed version of the simulant, this was to provide a valid basis for comparison. Ultimately, the JSC-1/1000/240 sample was selected. Due to the fact that no ilemnite is present in this simulant meaning that the iron reduction is caused from the reduction of silicate minerals, an event that has very few studies experimentally analysing. With JSC-1/1000/120 being selected, the unprocessed version is also selected for this analysis. Figure 5.27 displays the spectra which was formed from the transmission Mössbauer analysis.

Through this analysis the atomic mass percentage within the given samples were obtained. For the case of this study the appearance of metallic iron shall only be taken into account. It must be reiterated that this is a preliminary analysis and further work must be completed in order to gain a better understanding between the relationship of iron production and the corresponding optical spectra of the lunar simulants. Nevertheless, with regards to the atomic mass percentage within the samples that have currently been studied, the unprocessed JSC-1 sample contained 23.40% of npFe^0, a surprising appearance which will need further analysis. This alters in the JSC-1/1000/240 sample where the npFe^0 present is valued at 6.06%, this is accompanied with the presence of 38.61% of alpha-iron, a type of metallic iron which is not seen in the unprocessed JSC-1 sample. Evidently, an increase of metallic iron is apparent in the reduction of the JSC-1 simulant. As previously mentioned, further analysis will need to be accomplished in order to determine a definitive relationship between the optical spectra and the metallic iron present in the reduced samples. A relationship will be determined through more iterations of testing, on both the JSC-1/1000/240 and the unprocessed JSC-1 samples, along with the testing and study of the remaining samples which were discussed in this study.

By obtaining quantification of the metallic iron present in the processed sample. Plots, like the ones seen in the previous section – defining a relationship between reddening gradient and the reduction temperature can be obtained. This would generate the possibility to fit an equation to a relationship between reddening gradient and the quantity of metallic iron within the sample - ultimately aiding in the quantification of metallic iron in the surface of the Moon and remote sensing techniques.

Figure 5.27: Transmission Mössbauer analysis: conducted at room temperature, using a conventional constant acceleration spectrometer with 25mC, source of 57Co in Rh matrix.

(a) Unprocessed JSC-1

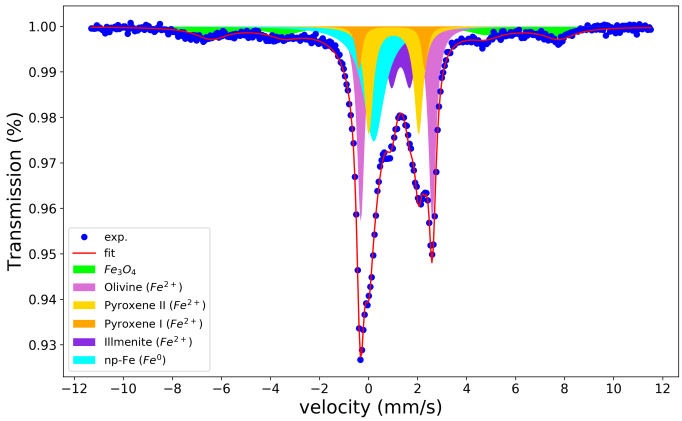

(b) JSC-1/1000/240

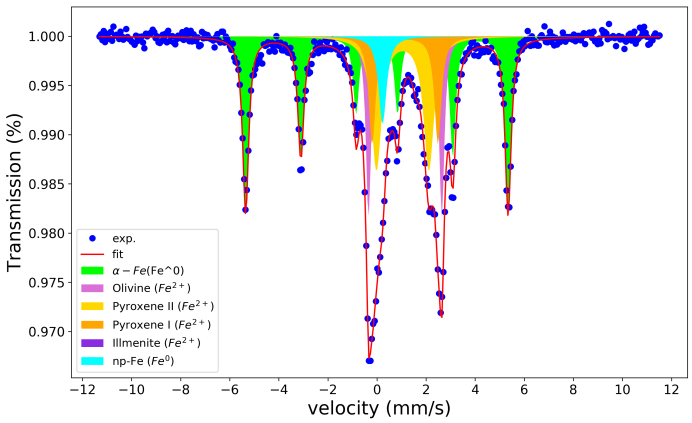

Chapter 6

Budget Summary

Defined in this section is the total economic cost for this thesis. This will include an accumulation of all the costing related to testing i.e. the process of testing the samples, the man power - the total time invested in completing each phase of this study and other costs. Below a budget breakdown is displayed of each phase in the study, concluding with the accumulation of the costing, present in table 6.1.

Table 6.1: Summary of Project's Budget

Phase of Study	**Costs**	
Hydrogen Reduction	Testing	€21.84
	Human Resources	€2,517.50
	Equipment	€5,337
	Other	€30.80
	Total	**€7,907.14**
SEM Characterisation	Testing	€426.96
	Human Resources	€620
	Equipment	-
	Other	€4.40
	Total	**€1,051.36**
UV-VIS Spectroscopy	Testing	€53.35
	Human Resources	€505
	Equipment	-
	Other	€6.60
	Total	**€564.95**
Mössbauer Analysis	Testing	€200
	Human Resources	€330
	Equipment	-
	Other	-
	Total	**€530**
Research and Analysis	Testing	-
	Human Resources	€16,827.50
	Equipment	€3000
	Other	-
	Total	**€19,827.50**
Total Cost for Project		**€29,880.95**

Testing

This area of the budget corresponds to the running cost of utilising the corresponding equipment to gain either the processed sample or raw data. It must be stated that the cost of the actual SEM equipment is not included, just the cost to use this equipment is present. This is also the case within the UV-VIS spectroscopy and Mössbauer analysis budget breakdown.

Human Resources

This area of the budget represents the time that is dedicated to each phase of this study. The Thesis is a 400 hour project, and as such the sum of the hours the student has dedicated to this project accumulates to 400 hours. Evidently, this sum excludes the time in which the project supervisor and the technicians – who aided in accomplishing the experimental phase of this project, have dedicated to this project.

Equipment

This area includes the equipment cost which was utilised through this experiment. Evident from table 6.1, only the equipment cost for research and analysis, and the hydrogen reduction phase is taken into account.

Other Costs

This are includes transportation related costs. Transportation represents the commutes conducted by the student to travel from their place of residence to the university campus.

Chapter 7

Analysis and Assessment of Environmental and Social Implications

The final aspect of the project is to discuss the potential impacts the results of this study has on both the environment and socially. These impacts are based off of future applications that this study possessed. First the possible environmental improvements shall be discussed, followed by the potential social impacts capable for this project.

7.1 Environmental Impact

Previously mentioned was the capabilities that one satellite has when exploring the surface of the Moon. To reiterate, up to 50% of the lunar surface was imaged by the Chandrayaan-1 satellite. Therefore, assuming that the Chandrayaan-1 satellite did cover 50% of the lunar surface it would only take two satellites to image the entire surface of the Moon. It is unknown how many rovers it would take in order to analyse the entire surface of the Moon, but it is safe to assume that that either it would take much more than two or take a much longer time to cover the lunar surface when comparing to two Chandrayaan-1 satellites. By significantly reducing the amount of resources needed to image the entire lunar surface i.e. just launching a couple satellites instead of sending multiple rovers, the required number of launches will also decrease. Assuming the launch used was the SpaceX Falcon 9, a launcher which according to an article released in 2019 produces 336,552kg of CO_2 per launch [62], the amount of CO_2 would also substantially decrease.

The future benefits of this project also correlates to an improvement in the environmental impact. Mainly, this project aids in locating lunar resources, more specifically metallic iron along with both water and oxygen. As a secondary objective a preliminary quantity is acquired for a specific hydrogen reduction process (referring to the observation made via the Mössbauer analysis). Only considering the main objective for this thesis, the method of locating lunar resources, this too has a positive impact on the environmental impact. Ultimately, by having an effective and efficient method in locating lunar resources the time in which needed between solely relying on imported resources (resources obtained via launches from Earth) and the initialisation of in-situ resource utilisation is far less. The needs for a human to survive in space with regards to oxygen and water intake is a well known fact, defined in [63] as being a total of 4.18kg per day (accumulation of oxygen, drinking water and water needed for food prep.). In terms of the lunar gateway, it

is planned to be the housing station for astronauts to sleep, conduct research and travel to the lunar surface. These missions are only aimed to be short duration missions, between 30 - 90 day crewed missions [64]. Assuming the maximum duration mission of 90 days the total water and oxygen required for 4 astronauts - the maximum number of crew members [64], is 1504kg. Estimating the production of water and oxygen gained via from the lunar regolith is 1kg a day the needed water and oxygen required to be transported by the launcher reduces to 1414kg. Subsequently, reducing the amount of propellant needed to launch and the CO_2 emitted via the launcher. It must be noted that the environmental impact induced by the setting up of the resource utilisation equipment and system is not taken into account. Additionally the effects that the metallic iron gained from the lunar regolith substituting a proportion of the materials transported via the launch is also not taken into account.

To summarise this discussion, the relationship between the results produced via this project, and extrapolating the potential of these results to the impact on the environment is defined by reducing the amount of greenhouse gasses during the launch phase of the mission. This includes: reducing the amount of equipment needed to analyse the entire surface of the Moon for lunar resources and minimising the time between being only reliant on important resources and partially reliant due to in-situ resources utilisation. Eventually, when in-situ resource utilisation is initialised the amount of mass dedicated to resources within the launcher is reduced along with the required propellant and emitted greenhouse gasses.

7.2 Social Impact

This project aims to address social issues in regards to societal education and initiating the infrastructure for space related companies. Through this project the overall knowledge of the reader will expand by understanding factors such as space weathering and the resources which are present on the Moon.

In addition to this, the reader will develop an understanding that sustainable bases are an achievable goal through obtaining space resources. Tackling employment and entrepreneur opportunities, before this project started research on space mining was conducted. Through this research an issue was seen for start ups with the aim to utilise space resources located on Near Earth Asteroids (NEA). Both companies Deep Space Industry (DSI) and Planetary Resources (PR) ran into this issue - the inability to make a sufficient cash flow to sustain the company. Ultimately leading to them being bought by other companies and diverting their attention to other projects [65]. This is due to the fact that the infrastructure in place for resource utilisation of asteroids in place and as such the aim of a company to utilise these resources is an extremely long term goal. Offering up the question, ”What needs to be in place to provide sufficient infrastructure for asteroid mining?”. This question has eventuated to viewing the effects of space weathering on the lunar regolith and providing reference for remote sensing to locate resources such as metallic iron, oxygen and water. How does this correspond to asteroid mining? Both the Moon and asteroids are airless bodies, both of which are exposed to space weathering effect. Therefore, with further development of this project - by quantifying the relationship seen between the presence of metallic iron and the optical properties generated, characterisation of these NEA’s would be an appropriate employment of the results generated through this and future related projects. By characterising NEA’s a database can form disseminating the quantities of resources present on inspected NEA’s allowing companies to reference and make the most profitable selection of the NEA’s to mine.

In summary the social impacts include, educating people and improving the understanding of the lunar surface and space weathering effects. The results of this project can eventually aid in the building an infrastructure for space mining. Providing the basis for companies to make the most profitable decision when selecting NEA's this will eventuate to seeing start ups with the aim to utilise space resources with the best possible chance to make a sufficient cash flow to maintain the company.

Chapter 8

Conclusion and Future Works

To conclude this project, this chapter aims to discuss the previously defined objectives that have been accomplished through the research and results obtained through this study. This will be accomplished by concluding the aspects found through this study. Additionally, a section dedicated to future work will be discussed in order to that the developments made throughout this study will increase in accuracy and produce more definitive solutions shall be discussed.

8.1 Conclusion

Through this study the following conclusions where determined:

- With regards to the composition of the lunar surface, it was determined through lunar samples gained from both the Apollo and luna missions, along with remote sensing from satellites like the M^3, the bulk chemistry that makes up the lunar surface. Through this data, it is seen that the mare contains the most amount of iron oxide. Therefore, this is the area in which holds the greatest possibility to obtain metallic iron, water, and subsequently oxygen.
- Through viewing the physical characteristics of both the lunar simulants analysed in this study, and the data obtained from in-situ lunar sample. It was found that both lunar simulants JSC-1, and FJS-3 provide a suitable substitution for in-situ lunar samples. It must be stated that further work will need to be completed in order to gain better knowledge on the physical characteristics of the lunar simulant FJS.
- By researching the various aspects of space weathering it has been defined in this study what constitutes as space weathering and the effects that it posses on the lunar surface. The key information to be taken from this study is the combination of solar winds and the heat events generated from the impact of micrometeorites causing an extremely reducing environment on the surface of the Moon. The products of this environment sees the formation of $npFe^0$ and SMFe within the surface grains of the lunar surface.
- By characterising the processed lunar simulants it was found that through the hydrogen reduction process - reducing JSC-1 and FJS-3 at 600°C, 800°C and 1000°C for 2 hours and 4 hours, the formation of $npFe^0$ and SMFe on the lunar simulants grain surfaces is confirmed. Demonstrating that the hydrogen reduction process implemented in this study mimics the products present from space weathering events.
- Evident from the UV-VIS spectroscopy analysis and the quantification of the reddening gradient seen throughout the produced spectra. There is a clear correlation

between the darkening and reddening reduction of the spectra, and the increasing reduction temperature implemented. Through the SEM characterisation of the lunar samples evidence suggest that there is increase quantities of metallic iron with increasing reduction temperature. Suggesting that the spectral changes seen correlates to increasing metallic quantities. In addition to this observation, an equation is fitted to the reddening gradient vs reduction temperature data points. This equation aims to demonstrate an preliminary mathematical model to predict the reddening gradient for a given reduction temperature.

- Through data gathered from the Mössbauer analysis there is evidence to suggest the theory of increase hydrogen reduction and increase in npFe^0/SMFe is correlated. Furthermore the data provided in this study offers the basis for further tests to be conducted in order to obtain an accurate quantification of the metallic iron present within the processed lunar simulants.

- Through the achievement of the primary objectives, the ability to expand the readers knowledge with regards to lunar resources and space weathering is achieved.

- A discussion has formed on the benefits that this project will have on future space exploration mission. With further development, a more definitive correlation between the optical spectra, within the UV spectrum, and metallic iron can form, subsequently forming a more accurate mathematical model which can later be implemented when remote sensing analysis is applied to the lunar surface and other airless bodies.

8.2 Future works

To further this study the first step must be followed. Provided through the Mössbauer analysis is a preliminary estimate of metallic iron content, produced from the hydrogen reduction process. This estimation will increase in accuracy through further iterations of the Mössbauer analysis. Following this the other samples will also follow the same Mössbauer analysis in order to determine the quantity of the metallic iron present in said samples. By determining the quantities of metallic iron in all of the samples the sample method, applied in chapter 5, section 2.3, an equation describing the reddening gradient and metallic iron content can form.

In order to increase the accuracy of the model created in this study, further experiments will need to be accomplished, with regards to processing the lunar simulants at an increased variety of reduction temperatures. This will increase the number of data points, subsequently defining a clearer correlation between the reddening gradient and reduction temperature. Moreover, by increasing the number of reduction temperatures a larger pool of metallic iron quantities will be obtained, improving the correlation seen between the reddening gradient and metallic iron content. With a more definitive correlation observed, an equation which better describes the relationship can be acquired. This will see the model improve its accuracy when interpolating data.

Bibliography

[1] 2020. URL: https://www.esa.int/Science_Exploration/Human_and_Robotic_Exploration/Exploration/Gateway.

[2] National Aeronautics and Space Administration. *The Artemis Plan: NASA's Lunar Exploration Program Overview*. 2020.

[3] C.M. Pieters and S.K. Noble. "Space weathering on airless bodies". In: *Journal of Geophysical Research: Planets* 121.10 (2016), pp. 1865–1884.

[4] C.M. Pieters et al. "The Moon mineralogy mapper (M^3) on chandrayaan-1". In: *Current Science* 96.4 (2009), pp. 500–505.

[5] D. Spreitzer and J. Schenk. "Reduction of iron oxides with hydrogen—a review". In: *Steel Research International* 90.10 (2019), p. 1900108.

[6] Y. Zhao and F. Shadman. "Production of oxygen from lunar ilmenite". In: *Resources of Near-Earth Space*. Ed. by J.S. Lewis, M.S. Matthews, and M.L. Guerrieri. 1993.

[7] H.M. Sargeant et al. "Feasibility studies for hydrogen reduction of ilmenite in a static system for use as an ISRU demonstration on the lunar surface". In: *Planetary and Space Science* 180 (2020), p. 104759. DOI: https://doi.org/10.1016/j.pss.2019.104759.

[8] U. Hegde et al. "Hydrogen reduction of lunar regolith simulants for oxygen production". In: *49th AIAA Aerospace Sciences Meeting including the New Horizons Forum and Aerospace Exposition*. 2011, p. 608.

[9] Y. Lu, D Mantha, and R.G. Reddy. "Thermodynamic Analysis on Lunar Soil Reduced by Hydrogen". In: *Metallurgical and Materials Transactions B* (2010), pp. 1543–1916. URL: https://doi-org.recursos.biblioteca.upc.edu/10.1007/s11663-010-9411-3.

[10] U. Hegde, R. Balasubramaniam, and S. Gokoglu. *Development of a Reactor Model for Chemical Conversion of Lunar Regolith*. Tech. rep. 2009-215626. Glenn Research Center Cleveland, Ohio 44135, Apr. 2009.

[11] U. Hegde, R. Balasubramaniam, and S. Gokoglu. "Development and Validation of a Model for Hydrogen Reduction of JSC–1A". In: *47th AIAA Aerospace Sciences Meeting including the New Horizons Forum and Aerospace Exposition*. Glenn Research Center Cleveland, Ohio 44135, May 2009.

[12] E.L. Christiansen, C. Simonds, and K.O. Fairchild. "Conceptual design of a lunar oxygen pilot plant". In: *Second Conference on Lunar Bases and Space Activities of the 21st Century*. Vol. 652. 1988, p. 52.

[13] W. Cassidy and B. Hapke. "Effects of darkening processes on surfaces of airless bodies". In: *Icarus* 25.3 (1975), pp. 371–383.

[14] S. Gou et al. "In situ spectral measurements of space weathering by Chang'E-4 rover". In: *Earth and Planetary Science Letters* 535 (2020), p. 116117.

[15] J.R. Gaier. “Optical Spectra of Lunar Dust Simulants”. In: (2018). URL: http://www.sti.nasa.gov/.

[16] P.G. Lucey, G.J. Taylor, and E. Malaret. “Abundance and distribution of iron on the Moon”. In: *Science* 268.5214 (1995), pp. 1150–1153.

[17] Dr. David R. Williams. NASA Goddard Space Flight Center, Greenbelt, MD 20771, 2020. URL: https://nssdc.gsfc.nasa.gov/planetary/clementine.html.

[18] P.G. Lucey, D.T. Blewett, and B.R. Hawke. “Mapping the FeO and TiO2 content of the lunar surface with multispectral imagery”. In: *Journal of Geophysical Research: Planets* 103.E2 (1998), pp. 3679–3699.

[19] E. Malaret and P.G. Lucey. “Medium Resolution Global Lunar Mosaics of FeO, TiO2 and Is/FeO”. In: *Lunar and Planetary Science Conference*. Vol. 27. 1996, pp. 797–798.

[20] D. Vaniman et al. “EXPLORATION, SAMPLES, AND RECENT CONCEPTS OF THE MOON”. In: *Lunar Sourcebook: a user’s guide to the moon*. Ed. by G. H. Heiken, D. T. Vaniman, and B. M. French. Cambridge University Press, 1991. Chap. 2.

[21] P.G. Lucey and M.A. Riner. “The optical effects of small iron particles that darken but do not redden: Evidence of intense space weathering on Mercury”. In: *Icarus* 212.2 (2011), pp. 451–462. ISSN: 0019-1035. DOI: https://doi.org/10.1016/j.icarus.2011.01.022. URL: https://www.sciencedirect.com/science/article/pii/S0019103511000339.

[22] B. Hapke, W. Cassidy, and E. Wells. “Effects of vapor-phase deposition processes on the optical, chemical, and magnetic properties OE the lunar regolith”. In: *The Moon* 13.1 (Mar. 1997), pp. 339–353. URL: https://doi.org/10.1007/BF00567525.

[23] C.C. Allen et al. “Microscopic Iron Metal on Glass and Minerals—A Tool for Studying Regolith Maturity”. In: *Icarus* 104.2 (1993), pp. 291–300. ISSN: 0019-1035. DOI: https://doi.org/10.1006/icar.1993.1102. URL: https://www.sciencedirect.com/science/article/pii/S0019103583711024.

[24] B. Hapke. “Space weathering from Mercury to the asteroid belt”. In: *Journal of Geophysical Research: Planets* 106.E5 (2001), pp. 10039–10073. DOI: https://doi.org/10.1029/2000JE001338. eprint: https://agupubs.onlinelibrary.wiley.com/doi/pdf/10.1029/2000JE001338. URL: https://agupubs.onlinelibrary.wiley.com/doi/abs/10.1029/2000JE001338.

[25] P.G. Lucey and S.K. Noble. “Experimental test of a radiative transfer model of the optical effects of space weathering”. In: *Icarus* 197.1 (2008), pp. 348–353.

[26] C.L. Li et al. “Detection and calibration characteristics of the visible and near-infrared imaging spectrometer in the Chang’e-4”. In: *Review of Scientific Instruments* 90.10 (2019), p. 103106. DOI: 10.1063/1.5089737. eprint: https://doi.org/10.1063/1.5089737. URL: https://doi.org/10.1063/1.5089737.

[27] R.V. Morris. “Origins and size distribution of metallic iron particles in the lunar regolith”. In: *Lunar and Planetary Science Conference Proceedings*. Vol. 11. 1980, pp. 1697–1712.

[28] H. Sato et al. “Lunar mare TiO2 abundances estimated from UV/Vis reflectance”. In: *Icarus* 296 (2017), pp. 216–238. ISSN: 0019-1035. DOI: https://doi.org/10.1016/j.icarus.2017.06.013. URL: https://www.sciencedirect.com/science/article/pii/S0019103516306595.

[29] W.D. Carrier III, G.R. Olhoeft, and W. Mendell. “PHYSICAL PROPERTIES OF THE LUNAR SURFACE”. In: *Lunar Sourcebook: a user’s guide to the moon*. Ed. by G.H. Heiken, D.T. Vaniman, and B.M. French. Cambridge University Press, 1991. Chap. 9, pp. 475–594.

[30] L.P. Keller and D.S. McKay. “The nature and origin of rims on lunar soil grains”. In: *Geochimica et Cosmochimica Acta* 61.11 (1997), pp. 2331–2341. ISSN: 0016-7037. DOI: https://doi.org/10.1016/S0016-7037(97)00085-9. URL: https://www.sciencedirect.com/science/article/pii/S0016703797000859.

[31] D.S. McKay et al. “THE LUNAR REGOLITH”. In: *Lunar Sourcebook: a user’s guide to the moon*. Ed. by G.H. Heiken, D.T. Vaniman, and B.M. French. Cambridge University Press, 1991. Chap. 7, pp. 285–356.

[32] B.N.Dwivedi and U. Narain. *Physics of the Sun and Its Atmosphere: Proceedings of the National Workshop (India) on ”Recent Advances in Solar Physics” : Meerut College, Meerut, India, 7-10 November, 2006*. World Scientific, 2008, p. 238. ISBN: 9789812832719. URL: https://books.google.co.uk/books?id=cPvSl4mX420C.

[33] R.M. Walker. “Nature of the fossil evidence - Moon and meteorites”. In: *The Ancient Sun: Fossil Record in the Earth, Moon and Meteorites*. Ed. by R. O. Pepin, J. A. Eddy, and R. B. Merrill. Jan. 1980, pp. 11–28.

[34] J. Borg et al. “Solar wind radiation damage in lunar dust grains and the characteristics of the ancient solar wind”. In: *The Ancient Sun: Fossil Record in the Earth, Moon and Meteorites*. Ed. by R. O. Pepin, J. A. Eddy, and R. B. Merrill. Jan. 1980, pp. 431–461.

[35] M.S. Thompson et al. “The oxidation state of nanophase Fe particles in lunar soil: Implications for space weathering”. In: *Meteoritics and Planetary Science* 51.6 (June 2016), pp. 1082–1095. ISSN: 10869379.

[36] M.J. Loeffler, C.A. Dukes, and R.A. Baragiola. “Irradiation of olivine by 4 keV He +: Simulation of space weathering by the solar wind”. In: *Journal of Geophysical Research E: Planets* 114.3 (Mar. 2009), pp. 1865–1872. ISSN: 01480227.

[37] N.F.M.N. Cabrera and N.F. Mott. “Theory of the oxidation of metals”. In: *Reports on progress in physics* 12.1 (1949), pp. 163–184.

[38] R.V. Morris et al. *Handbook of Lunar Soils*. 19069. NASA Johnson Space Center, Houston: Johnson Space Center, 1983.

[39] H. Heywood. “Particle size and shape distribution for lunar fines sample 12057, 72”. In: *Lunar and Planetary Science Conference Proceedings*. Vol. 2. 1971, pp. 1989–2001.

[40] H. Gorz et al. “Particle size and shape distributions of lunar fines by CESEMI”. In: *Lunar and Planetary Science Conference Proceedings*. Vol. 2. 1971, p. 2021.

[41] H. Gorz et al. “CESEMI studies of Apollo 14 and 15 fines”. In: *Lunar and Planetary Science Conference Proceedings*. Vol. 3. 1972, p. 3195.

[42] A. Mahmood, J.K. Mitchell, and W.D. Carrier III. “Grain orientation in lunar soil”. In: *Lunar and Planetary Science Conference Proceedings*. Vol. 5. 1974, pp. 2347–2354.

[43] D.A. Cadenhead et al. “Some surface area and porosity characterizations of lunar soils”. In: *Lunar and Planetary Science Conference Proceedings*. Vol. 8. 1977, pp. 1291–1303.

[44] 2021. URL: https://www.chem.fsu.edu/chemlab/chm1046course/solids.html.

[45] J.J. Papike, S.B. Simon, and J.C. Laul. “The lunar regolith: Chemistry, mineralogy, and petrology”. In: *Reviews of Geophysics* 20.4 (1982), pp. 761–826.

[46] D.S. McKay et al. “JSC-1: A new lunar soil simulant”. In: *Engineering, construction, and operations in space IV 2* (1994), pp. 857–866.

[47] S. Li et al. “Widespread hematite at high latitudes of the Moon”. In: *Science advances* 6.36 (2020), eaba1940.

[48] E.J. Garboczi. “Three dimensional shape analysis of JSC-1A simulated lunar regolith particles”. In: *Powder Technology* 207.1-3 (2011), pp. 96–103.

[49] H. Kanamori et al. “Properties of Lunar Soil Simulant Manufactured in Japan”. In: *Space 98*. 1998, pp. 462–468. DOI: 10.1061/40339(206)53. eprint: https://ascelibrary.org/doi/pdf/10.1061/40339\%28206\%2953. URL: https://ascelibrary.org/doi/abs/10.1061/40339%5C%28206%5C%2953.

[50] 2018. URL: https://simulantdb.com/simulants/fjs.php.

[51] T. Matsushima et al. “3D Shape Characterization and Image-Based DEM Simulation of the Lunar Soil Simulant FJS-1”. In: *Journal of Aerospace Engineering* 22.1 (2009), pp. 15–23. DOI: 10.1061/(ASCE)0893-1321(2009)22:1(15). eprint: https://ascelibrary.org/doi/pdf/10.1061/\%28ASCE\%290893-1321\%282009\%2922\%3A1\%2815\%29. URL: https://ascelibrary.org/doi/abs/10.1061/%5C%28ASCE%5C%290893-1321%5C%282009%5C%2922%5C%3A1%5C%2815%5C%29.

[52] https://jpl.nasa.gov. *Moon Mineralogy Mapper - Moon Instruments - NASA Jet Propulsion Laboratory*. 2020. URL: https://www.jpl.nasa.gov/missions/moon-mineralogy-mapper-m3.

[53] S. Aggarwal. “Principles of remote sensing”. In: *Satellite remote sensing and GIS applications in agricultural meteorology* 23 (2004). Ed. by M.V.K. Sivakumar et al., pp. 23–28.

[54] D. Liu et al. “An Empirical Model to Estimate Abundance of Nanophase Metallic Iron (npFe0) in Lunar Soils”. In: *Remote Sensing* 12.6 (2020), p. 1047.

[55] M. Skorianz. “Classification of iron ores regarding their reduction behavior in fluidized bed technologies”. PhD thesis. Franz-Josef-Straße 18 – 8700 Leoben, Austria: Montanuniversitaet Leoben/Chair of Metallurgy, Oct. 2012, pp. 11–32.

[56] G.P. Thomson and A. Reid. “Diffraction of cathode rays by a thin film”. In: *Nature* 119.3007 (1927), pp. 890–890.

[57] Kannan M. “Scanning Electron Microscopy: Principle, Components and Applications”. In: *A Textbook on Fundamentals and Applications of Nanotechnology*. Mar. 2018. Chap. 8, pp. 81–92. ISBN: 978-93-5124-932-0 (PB).

[58] R.F. Egerton and et al. *Physical principles of electron microscopy*. Vol. 56. Springer, 2005. Chap. 1.

[59] Oxford Instruments. “INCA Energy Operator Manual”. In: *High Wycombe: Oxford Instruments Analytical Ltd* (2006).

[60] Shimadzu Corp. *UV-3600, Shimadzu UV-VIS-NIR spectrophotometer*. URL: http://www.shimadzu.com.

[61] R.F. Kokaly et al. *USGS Spectral Library Version 7*. 2017. DOI: https://doi.org/10.3133/ds1035.

[62] Lloyd Alter. *A SpaceX Launch Puts Out as Much CO2 as Flying 341 People Across the Atlantic*. 2019. URL: https://www.treehugger.com/spacex-launch-puts-out-much-co-flying-people-across-atlantic-4857958.

[63] M. Ewert and C. Stromgren. “Astronaut Mass Balance for Long Duration Missions”. In: 49th International Conference on Environmental Systems. 2019.

[64] W. Gerstenmaier and J. Crusan. “Cislunar and Gateway Overview”. In: *HEO Committee of the NASA Advisory Council Meeting*. Mountain View, CA: Ames Research Center (ARC), 2018.

[65] J. Foust. *The Space Review: The Asteroid Mining Bubble has Burst*. Jan. 2019. URL: https://www.thespacereview.com/article/3633/1.